
EXPLORING THE POTENTIAL OF HYBRID MACHINE-LEARNING/PHYSICS-BASED MODELING FOR ATMOSPHERIC/OCEANIC PREDICTION BEYOND THE MEDIUM RANGE

A PREPRINT

Dhruvit Patel*
Department of Physics
University of Maryland
College Park, MD, USA
dpp94@uchicago.edu

Troy Arcomano
Argonne National Laboratory
Lemont, IL, USA
tarcomano@anl.gov

Brian Hunt
Institute for Physical Science and Technology
University of Maryland
College Park, MD, USA

Istvan Szunyogh
Department of Atmospheric Sciences
Texas A&M University
College Station, TX, USA

Edward Ott
Department of Physics
Department of Electrical and Computer Engineering
University of Maryland
College Park, MD, USA

May 31, 2024

ABSTRACT

This paper explores the potential of a hybrid modeling approach that combines machine learning (ML) with conventional physics-based modeling for weather prediction beyond the medium range. It extends the work of Arcomano et al. [2022], which tested the approach for short- and medium-range weather prediction, and the work of Arcomano et al. [2023], which investigated its potential for climate modeling. The hybrid model used for the forecast experiments of the paper is based on the low-resolution, simplified parameterization atmospheric general circulation model (AGCM) SPEEDY. In addition to the hybridized prognostic variables of SPEEDY, the current version of the model has three purely ML-based prognostic variables. One of these is 6 h cumulative precipitation, another is the sea surface temperature, while the third is the heat content of the top 300 m deep layer of the ocean. The model has skill in predicting the El Niño cycle and its global teleconnections with precipitation for 3-7 months depending on the season. The model captures equatorial variability of the precipitation associated with Kelvin and Rossby waves and MJO. Predictions of the precipitation in the equatorial region have skill for 15 days in the East Pacific and 11.5 days in the West Pacific. Though the model has low spatial resolution, for these tasks it has prediction skill comparable to what has been published for high-resolution, purely physics-based, conventional operational forecast models.

Plain Language Summary

This paper is an assessment of the potential of a hybrid modeling approach for weather prediction beyond 7-10 days. This approach combines machine learning (ML) with a conventional physics-based model of the atmospheric general circulation. Some ML components of the hybrid model make corrections to the prognostic variables of the conventional model. Other components provide information about the changes in the sea surface temperature that result from interactions between the atmosphere and ocean, or provide enhanced capabilities for the prediction of the precipitation.

*Now at the Department of Geophysical Sciences at the University of Chicago.

The results of forecast experiments with the model show that it has skill in predicting the El Niño cycle and its influence on the weather in other parts of the world for 3-7 months depending on the season. The model also provides useful forecast information about the precipitation in the Tropics for 11-15 days depending on the location. The tested approach could be used both to hybridize current high-resolution purely physics-based operational models and to enhance the capabilities of low-resolution models of the general circulation used in academic research.

1 Introduction

Steady progress in weather prediction beyond the medium (7-10 days) forecast range has been made in numerical weather prediction (NWP) (e.g., National Academies of Sciences and Engineering and Medicine [2016], White et al. [2022]). Advances in land and ocean modeling have been crucial for these improvements (Brassington et al. [2015]). Both the European Centre for Medium-Range Weather Forecasts (ECMWF) (Vitart [2014]) and the National Centers for Environmental Prediction (NCEP) (Saha et al. [2014]) have coupled ocean-atmosphere ensemble-based systems, with predictions extending well beyond 10 days lead time. However, the longer range forecasts prepared with these systems tend to have substantial biases (e.g., Zhang et al. [2021], White et al. [2017], Molod et al. [2020], Moutadid et al. [2023], Monhart et al. [2018], Domeisen et al. [2022]). Improved modeling of the atmosphere-land-sea-ice interfaces and tropical convection (e.g., convection-coupled equatorial waves) has long been considered pivotal for gaining forecast skill beyond the medium range (e.g., Zhang [2013]). Using machine learning-based (ML-based) model components is one promising avenue to achieve this goal, with the additional benefit that such model components can also substantially reduce the computational cost associated with fully coupled, purely physics-based models.

Current ML-based weather forecasting models have demonstrated skill comparable to, or even surpassing, that of the operational Integrated Forecasting System (IFS) of ECMWF in the 1 day to 10 days forecast range (e.g., Bi et al. [2023], Lam et al. [2023], Chen et al. [2023a,c], Nguyen et al. [2023]). While it is less clear that these ML-based models are also suitable for prediction beyond the medium range (Chattopadhyay and Hassanzadeh [2023]), there have been some promising initial attempts to show that this may be the case. For instance, Weyn et al. [2021] showed that an ensemble prediction system based on an ML model of 6 prognostic variables provided ensemble mean forecasts that were only modestly inferior to the ECMWF ensemble mean forecasts in the 4 to 6 weeks forecast range. More recently, the FuXi-S2S model, the first ML-only based model designed specifically for forecasting beyond the medium range (Chen et al. [2023b]), was shown to perform on par, or slightly better, than the ensemble mean of the ECMWF system for precipitation anomaly and Madden-Julian oscillation (MJO) forecasts out to 6 weeks. However, this 6 week time scale is not long enough to take advantage of the potential predictability associated with teleconnections of the El Niño.

The incorporation of machine learning into existing conventional physics-based forecast models is appealing because it takes advantage of both the vast physics-based knowledge built into those models and the availability of decades-long time series of observation-based analyses of the atmospheric states, which can be used for ML training. Hybrid models implementing such an approach have been shown to be stable during decades-long simulations, reduce biases of the host atmospheric general circulation model, and improve weather forecasts (Watt-Meyer et al. [2021], Arcomano et al. [2022, 2023], Kochkov et al. [2023], Kwa et al. [2023]). Arcomano et al. [2023] (AEA23 hereafter) described a hybrid model in which the atmospheric component was a low-resolution AGCM hybridized with ML, while the oceanic component was a purely ML-based model of the sea surface temperature (SST). This model stably produced realistic atmospheric states and SST fields in a 70-year simulation, significantly reducing the atmospheric biases of the host AGCM, while also better capturing the temporal variability of the atmospheric states. It also reproduced many important features of the observed SST climatology with good accuracy, including the variability associated with El Niño. The variability and low biases of the hybrid model were comparable with those of high-resolution physics-based climate models, though the hybrid model requires only modest computational resources to train and run.

Here we present results obtained with a new version of the model of AEA23. This new version of the model has better forecast skill than the original model at forecast lead times longer than 7 days. The new features of the model that led to this improvement of the forecast skill are an ML-based prognostic variable for the heat content of the top 300 m layer of the ocean, and capabilities to handle disparate time scales of the atmospheric and oceanic dynamics. As in AEA23, the AGCM is the Simplified Parameterization, primitive-Equation Dynamics (SPEEDY) model (Molteni [2003], Kucharski et al. [2006]). The low resolution of this AGCM allowed us to relatively rapidly test many different configurations of the hybrid model, because retraining the model requires only modest computational resources that are available at many academic institutions.

The structure of the paper is as follows. Section 2 summarizes the hybrid methodology and the changes made to the AEA23 model. Section 3 discusses the data used in the numerical experiments for both training and assessing the forecast performance of the model. Section 4 demonstrates the forecast capabilities of the model, examining its predictive skill for various atmospheric and oceanic phenomena based on 195 experimental 2-year forecasts. The main result is that the model has useful forecast skill well beyond the medium range. Specifically, the model has skill in

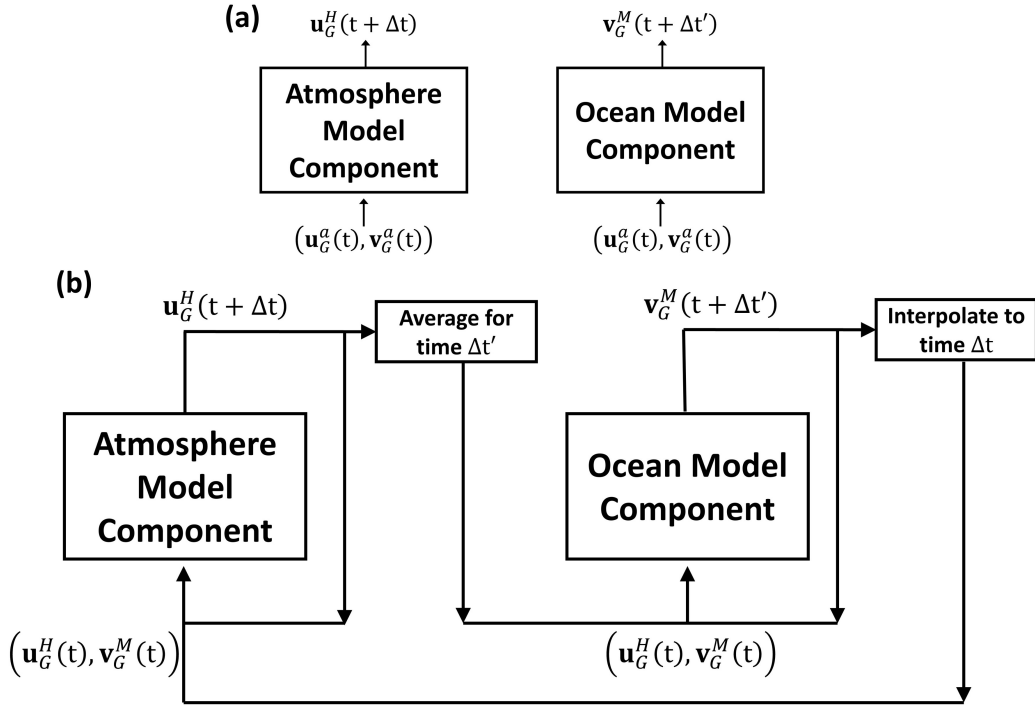


Figure 1: Schematic of the model setup during (a) training and (b) prediction. The atmospheric model component and ocean model component are trained independently as shown in (a), but coupled during prediction as shown in (b). We take the atmospheric (oceanic) model state $\mathbf{u}_G(t)$ ($\mathbf{v}_G(t)$) to be $\mathbf{u}_G^a(t)$ ($\mathbf{v}_G^a(t)$) during training and $\mathbf{u}_G^H(t)$ ($\mathbf{v}_G^M(t)$) during prediction. The super-script a denotes the observation-based analysis atmospheric or oceanic states, and the super-script H (M) denotes the states predicted by the hybrid atmospheric (ML-only oceanic) model component. Since the time step Δt of the atmospheric model component is taken to be smaller than the time step $\Delta t'$ of the oceanic model component (i.e., $\Delta t' = n\Delta t$), the atmospheric model component variables used as input to the oceanic model component are time-averaged over a trailing $n\Delta t$ time window. In a similar fashion, the oceanic model component variables fed to the atmospheric model component are interpolated in time to produce the Δt time step of the oceanic input to the atmospheric model component. See Sec. 2.2 for more details.

predicting El Niño and its global precipitation teleconnections for 3-7 months depending on the season. The model can also maintain variability of the precipitation associated with equatorial Kelvin and Rossby waves and also in the wavelength-frequency range of MJO for the entire 2-year duration of the forecasts. In addition, the forecasts of the precipitation anomalies in the equatorial region have skill for 15 days in the East Pacific and 11.5 days in the West Pacific. Section 5 presents further discussion and the conclusions.

2 Methods

Our model has the same hybrid architecture and it is also trained by the same protocol as the model of AEA23. It has two major components: (1) a hybrid component for the atmosphere that combines SPEEDY with an ML model, and (2) an ML-only component for the ocean. We denote the vector of the atmospheric prognostic state variables by $\mathbf{u}_G(t)$ and the vector of the oceanic prognostic state variables by $\mathbf{v}_G(t)$. The two model components are coupled by using both $\mathbf{u}_G(t)$ and $\mathbf{v}_G(t)$ as input to both of them (see Fig. 1). Though they are trained separately to make one time step forward predictions $\mathbf{u}_G(t + \Delta t)$ and $\mathbf{v}_G(t + \Delta t')$, they interact nonlinearly in the predictions, in which the outputs $\mathbf{u}_G(t + \Delta t)$ and $\mathbf{v}_G(t + \Delta t')$ serve as the inputs of the next time step (Fig. 1). Note, that the time steps Δt and $\Delta t'$ of the atmospheric model component and oceanic model component, respectively, may be different. For the results we report, we use time step $\Delta t = 6$ hours for the hybrid atmospheric component and $\Delta t' = 72$ hours for the ML-only oceanic component. The details of training and prediction are discussed in Sec. 2.2.

The model grid of both model components is divided into local sub-domains: For the atmospheric model, each sub-domain is a vertical column extending from the lowest to the highest atmospheric model level, with a rectangular base (see the blue box in Fig. 2). For the ocean model, each sub-domain is just the rectangular base of an atmospheric

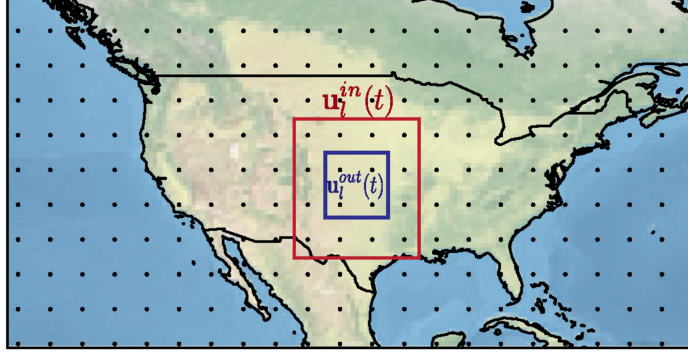


Figure 2: Illustration of the geographic domain decomposition for a local input vector $\mathbf{u}_l^{(in)}$ (with grid points enclosed by a red box), and a local output vector $\mathbf{u}_l^{(out)}$ (with grid points enclosed by a blue box).

subdomain (i.e., the ocean model is two-dimensional). The basic units of the ML model are reservoir computers (Jaeger [2001], Lukoševičius and Jaeger [2009], Lukoševičius [2012]), and each sub-domain is modeled by an individual and independently-trained reservoir computer (Pathak et al. [2018a]). This architecture allows the ML model training to be parallelized, therefore effectively utilizing the resources of a high performance computing (HPC) environment. The atmospheric hybrid component is constructed according to the Combined Hybrid-Parallel Prediction (CHyPP) approach for modeling large and complex spatiotemporally chaotic systems (Pathak et al. [2018b], Wikner et al. [2020]), in which a single global knowledge-based model (in our case, SPEEDY) is combined with a data-driven ML model composed of locally-connected individual reservoir computers. Below we describe the details of the model architecture, and its operation during the training and prediction phases.

2.1 The Global and Local State Vectors

For our hybrid atmospheric model we adopt the spatial discretization of the global domain that is used by the physics-based numerical model SPEEDY. While SPEEDY is a spectral transform model, it uses a discretized spatial grid with horizontal grid spacing of $3.75^\circ \times 3.75^\circ$ (so $n_h = 96 \times 48 = 36,864$ horizontal grid points (black dots in Fig. 2)) to represent the input and output model state and to compute the nonlinear and parameterized terms of the physics-based prognostic equations. The SPEEDY model state consists of the two components of the three-dimensionally varying horizontal wind, the three-dimensionally varying temperature and specific humidity fields, and the two-dimensionally varying (natural logarithm of) surface pressure. The three-dimensionally varying state variables are defined at $n_v = 8$ vertical σ -levels (at $\sigma = 0.025, 0.095, 0.20, 0.34, 0.51, 0.685, 0.835, \text{ and } 0.95$), where σ is the ratio of pressure to the surface pressure. We add to the notation of the grid-based global atmospheric state vector \mathbf{u}_G the super-script P to represent the SPEEDY model state \mathbf{u}_G^P , the super-script H to represent the hybrid atmospheric model state \mathbf{u}_G^H , and the super-script a to represent the observation-based analysis (estimate) \mathbf{u}_G^a of \mathbf{u}_G . In addition to the prognostic variables of SPEEDY, \mathbf{u}_G^H can include additional prognostic variables. In our current version of the model, there is one such prognostic variable: $\ln(10^3 P + 1)$, where P is the 6-h cumulative precipitation in units of meters. This prognostic variable is a purely ML-based state variable rather than a hybridized state variable based on the diagnostic precipitation variable of SPEEDY.

The same transformed variable for the cumulative precipitation was used before in ML-based weather prediction models by Pathak et al. [2022] and Rasp et al. [2018]. We take \mathbf{u}_G to be \mathbf{u}_G^a during training and \mathbf{u}_G^H during prediction. (See Fig. 1 and refer to Sec. 2.2 for further details.)

The ML-only oceanic component of the model uses the same horizontal grid as the hybrid atmospheric component. The elements of the ocean model state vector are the grid values of the two-dimensionally varying fields of the SST and the heat content of the top 300 m layer of the ocean. We add the super-script a to the notation of the grid-based global oceanic state vector \mathbf{v}_G , which represents the aforementioned two fields as a single vector, to denote its observation-based estimate \mathbf{v}_G^a . We add the super-script M to \mathbf{v}_G to denote the ML-only oceanic model state \mathbf{v}_G^M . We take \mathbf{v}_G to be \mathbf{v}_G^a during our model training, and \mathbf{v}_G^M during prediction (see Fig. 1). We note that heat content is an internal variable of the oceanic component of the model, because only the SST field serves as input to the atmospheric component.

We partition the global horizontal domain into $L = 1,152$ sub-domains. Each sub-domain l has a $7.5^\circ \times 7.5^\circ$ base of 4 grid points (see the black dots enclosed by the blue box in Fig. 2) and the subdomains for the atmosphere include the

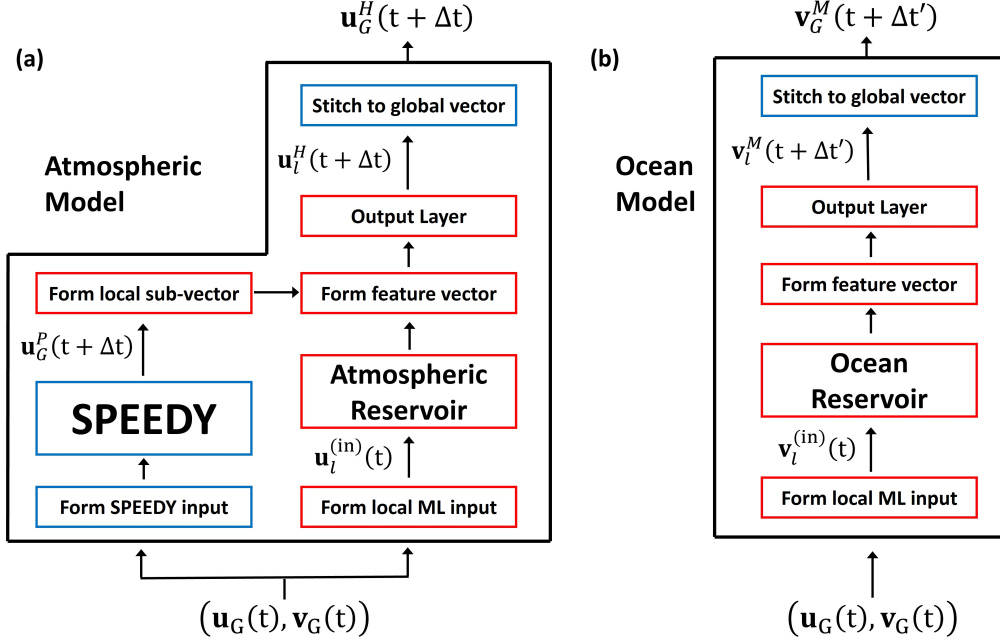


Figure 3: Model architecture flow chart for the (a) hybrid atmospheric component, and (b) ML-only oceanic component. The notation is explained in detail in Sec. 2.1 and Sec. 2.2. Red boxes represent operations that are performed locally (and in parallel) on each of the $L = 1, 152$ sub-domains. Blue boxes represent operations for which the outputs are global state vectors. Both model components receive $\mathbf{u}_G(t)$ and $\mathbf{v}_G(t)$ as input. The hybrid atmospheric (ML-only oceanic) component produces $\mathbf{u}_G^H(t + \Delta t)$ ($\mathbf{v}_G^M(t + \Delta t')$) as output, by stitching together local forecasts $\mathbf{u}_l^H(t + \Delta t)$ ($\mathbf{v}_l^M(t + \Delta t')$). In practice, the ocean model time step is larger than the atmospheric model time step, and for time steps where the ocean model is not advanced, the ocean model state is held constant.

n_v σ -levels specified by SPEEDY. Let \mathbf{u}_l , \mathbf{u}_l^P and \mathbf{u}_l^H be the local sub-vectors of \mathbf{u}_G^P , \mathbf{u}_G^P and \mathbf{u}_G^H , respectively, which consist of the elements of the related global state vectors that represent the atmospheric state in sub-domain l . Likewise, let \mathbf{v}_l and \mathbf{v}_l^M be the sub-vectors of \mathbf{v}_G and \mathbf{v}_G^M that represent the oceanic state in sub-domain l . In addition, we define \mathbf{u}_l^a and \mathbf{v}_l^a to be the observation-based analyses (estimates) of \mathbf{u}_l and \mathbf{v}_l .

The different state variables can have different units and ranges (possibly separated by orders of magnitude), and for a given state variable the range can also vary with the geographic location and altitude. To avoid artificially under-emphasizing or over-emphasizing any particular state variable in the training of the ML components, at each grid point in a sub-domain l we re-scale each state variable by subtracting the climatological mean and dividing by the climatological standard deviation of that state variable over all corresponding horizontal grid points at that altitude in sub-domain l and over all time points in the training data. The re-scaled state variables are then used to form the local state vectors that are used as input to the ML-components of the model during training and when making predictions.

The following subsections 2.2 to 2.5 provide detailed descriptions of the setup of our system outlined in the present subsection 2.1. A reader more interested in our results may choose to initially skip subsections 2.2 to 2.5, as the rest of the paper (Secs. 3 to 5) should still be understandable.

2.2 ML Model Dynamics

The basic units of the ML-based components of the model are reservoir computers. These units advance the ML-based component of the local atmospheric state vectors $\mathbf{u}_l^H(t)$ as well as the full local oceanic state vectors $\mathbf{v}_l^M(t)$ in time. In principle, the reservoir computing (RC) time step can be different for the atmosphere and ocean (i.e., for $\mathbf{u}_l^H(t)$ and $\mathbf{v}_l^M(t)$). We choose the time step $\Delta t'$ for the ocean to be larger than the time step Δt for the atmosphere by an integer multiple n (i.e., $\Delta t' = n\Delta t$). When the oceanic component makes a $\Delta t'$ -step forward forecast for time $t + \Delta t'$ starting at time t , the atmospheric component makes n successive Δt -step forward forecasts starting at time t . During the n Δt -step forward atmospheric forecasts, the ocean model state is held constant. (We have experimented only with values of Δt that have been substantially larger than the numerical integration time step for the physics-based SPEEDY model.) To propagate information about the state between subdomains, the RC inputs at time t for the prediction of

$\mathbf{u}_l(t + \Delta t)$ and $\mathbf{v}_l(t + \Delta t')$ describe the states in a local region that is extended in the horizontal directions (see the red box in Fig. 2).

In addition to the components that describe the atmospheric state in the extended local region, the input vector $\mathbf{u}_l^{(in)}(t)$ (Fig. 3(a)) for the prediction of $\mathbf{u}_l(t + \Delta t)$ also includes the SST components of $\mathbf{v}_l(t)$ from the extended local region and additional prescribed components that represent the incoming solar radiation at the top of the atmosphere. The reservoir computer for each sub-domain l has an internal state vector of dimension N that we denote $\mathbf{r}_l(t) = [r_1(t), r_2(t), \dots, r_N(t)]^T$ (see the red box labeled ‘‘Atmospheric Reservoir’’ in Fig. 3). This reservoir state evolves in time according to the following recurrent equation, driven by the corresponding local m -dimensional input vector $\mathbf{u}_l^{(in)}(t)$ of that sub-domain,

$$\mathbf{r}_l(t + \Delta t) = (\mathbf{I} - \mathbf{C}_l)\mathbf{r}_l(t) + \mathbf{C}_l \tanh(\mathbf{A}_l\mathbf{r}_l(t) + \mathbf{B}_l\mathbf{u}_l^{(in)}(t)). \quad (1)$$

where \mathbf{B}_l is a $N \times m$ sparse matrix with only one nonzero element per row, and such that each column has the same number of nonzero elements. The nonzero elements of \mathbf{B}_l are randomly chosen from a uniform distribution over the interval $[-b, b]$. The matrix \mathbf{A}_l is called the reservoir network adjacency matrix and is generated as a $N \times N$ sparse, random matrix with an average of d nonzero matrix elements in each row and each column (we refer to d as the ‘‘nodal degree’’). It is then re-scaled by dividing each element by the spectral radius ρ of the matrix. (The spectral radius of \mathbf{A}_l is the magnitude of its largest eigenvalue.) The matrix \mathbf{I} is a $N \times N$ identity matrix, and the ‘‘leaking rate matrix’’ $\mathbf{C}_l = \text{diag}(c_1, c_2, \dots, c_N)$ is a diagonal matrix of leaking rates that determine the amount of memory retained by the current reservoir state of the past reservoir states. The ‘‘activation function’’ $\tanh(\cdot)$ is an N -vector formed from the N scalars obtained by the tanh operating element-wise on its N -vector argument.

The local reservoir state $\mathbf{r}_l(t + \Delta t)$ at time $t + \Delta t$ is linearly mapped to the local model state at time $t + \Delta t$ according to

$$\mathbf{u}_l^H(t + \Delta t) = \mathbf{W}_l\tilde{\mathbf{r}}_l(t + \Delta t) = \mathbf{W}_l \begin{bmatrix} \mathbf{u}_l^P(t + \Delta t) \\ \chi(\mathbf{r}_l(t + \Delta t)) \end{bmatrix}, \quad (2)$$

where \mathbf{W}_l is an output weight matrix of trainable parameters, $\tilde{\mathbf{r}}_l$ is the augmented atmospheric model reservoir state for sub-domain l , and $\chi(\cdot)$ squares every other element of its vector-valued argument (e.g., for $\mathbf{x} = [x_1, x_2, x_3, x_4, \dots]^T$, $\chi(\mathbf{x}) = [x_1, x_2^2, x_3, x_4^2, \dots]^T$) (Patel and Ott [2023], Pathak et al. [2018a]). Additionally, for the hybrid atmospheric model $\mathbf{W}_l = [\mathbf{W}_l^P \quad \mathbf{W}_l^R]$. $\mathbf{u}_l^P(t + \Delta t)$ is obtained from $\mathbf{u}_G^P(t + \Delta t)$, which is obtained by making a Δt time step forecast with SPEEDY using $\mathbf{u}_G^P(t)$ as the initial condition.

For the ML-only ocean component, in addition to the vector components that describe the oceanic state in the extended local region, the input vector $\mathbf{v}_l^{(in)}(t)$ (Fig. 3(b)) for the prediction of $\mathbf{v}_l(t + \Delta t')$ also includes the vector components of $\mathbf{u}_l(t)$ corresponding to the lowest atmospheric model level from the extended local region and additional prescribed components that represent the incoming solar radiation at the top of the atmosphere. (We implement a simple land/ocean mask in the following way. Only sub-domains that contain at least one grid point located over an ocean are assigned a local ocean reservoir for predicting the local oceanic state. If the sub-domain contains a mix of land and ocean grid points, the elements of the local oceanic state vector corresponding to the ‘‘SST’’ values at land grid points are set to 272.0K and the elements of the local oceanic state vector corresponding to the ‘‘top 300m ocean heat content’’ at land grid points are set to 0 Jm⁻², during both training and prediction. Specifically, for prediction, the local reservoir for such a sub-domain does predict the ‘‘SST’’ and ‘‘top 300m ocean heat content’’ values at the land grid points, but this prediction is overwritten by setting that value to 272.0K for the SST and to 0 Jm⁻² for the top 300m ocean heat content.) The local reservoir state vector $\mathbf{r}'_l(t)$ of the ocean reservoir corresponding to sub-domain l (see the red box labeled ‘‘Ocean Reservoir’’ in Fig. 3(b)) evolves according to the following recurrent equation, driven by the corresponding local input vector $\mathbf{v}_l^{(in)}(t)$ of that sub-domain,

$$\mathbf{r}'_l(t + \Delta t') = (\mathbf{I} - \mathbf{C}'_l)\mathbf{r}'_l(t) + \mathbf{C}'_l \tanh(\mathbf{A}'_l\mathbf{r}'_l(t) + \mathbf{B}'_l\mathbf{v}_l^{(in)}(t)), \quad (3)$$

where the prime notation is used to emphasize that the ML components of the hybrid atmospheric prognostic equations and the ML-only oceanic prognostic equations use independent reservoirs (see the separate branches for computations for the atmospheric and oceanic models with separate ‘‘Atmospheric Reservoir’’ and ‘‘Ocean Reservoir’’ in Fig. 3). The local oceanic model state $\mathbf{v}_l^M(t + \Delta t')$ is then calculated as

$$\mathbf{v}_l^M(t + \Delta t') = \mathbf{W}'_l\tilde{\mathbf{r}}'_l(t + \Delta t') = \mathbf{W}'_l\chi(\mathbf{r}'_l(t + \Delta t')). \quad (4)$$

Equations (3) and (4) are applied only when t is a multiple $\Delta t' = n\Delta t$. In order that $\mathbf{v}_l^M(t)$ be defined at every time step of the atmospheric model component, we define $\mathbf{v}_l^M(t + j\Delta t) = \mathbf{v}_l^M(t + n\Delta t)$ for $j = 1, 2, \dots, n - 1$ whenever t is a multiple of $\Delta t'$. This represents a particularly simple form of the interpolation depicted in Fig. 1(b). The parameters of the output weight matrices \mathbf{W}_l and \mathbf{W}'_l are learned from reanalysis data during training, the details of which are outlined in the next subsection.

2.3 Model Training

For a sub-domain l of the atmospheric model, the objective of the ML training is as follows. Given target training data $\mathbf{u}_l^a(k\Delta t)$ at times $k\Delta t$ for $k = -K, -K + 1, -K + 2, \dots, 0$, determine parameters \mathbf{W}_l for which the one-step forward model forecasts best fit the training data in a least-squares sense. This is done by minimizing the following cost function,

$$J(\mathbf{W}_l) = \sum_{k=-K+K_T}^0 \|\mathbf{W}_l \tilde{\mathbf{r}}_l(k\Delta t) - \mathbf{u}_l^a(k\Delta t)\|^2 + \beta \|\mathbf{W}_l\|^2, \quad (5)$$

where the adjustable Tikhonov regularization parameter β is included to prevent over-fitting (Tikhonov and Arsenin [1977]), and K_T denotes the number of samples that are discarded as transients. Note, the reservoir computers of all sub-domains are trained independently in an identical manner (see the blue box in Fig. 3). For the hybrid prognostic equations, the solution to the minimization problem is

$$\mathbf{W}_l = \begin{pmatrix} \mathbf{U}_l^a (\mathbf{U}_l^P)^T & \mathbf{U}_l^a \mathbf{R}^T \end{pmatrix} \begin{bmatrix} \mathbf{U}_l^P (\mathbf{U}_l^P)^T + \beta^P \mathbf{I} & \mathbf{U}_l^P \mathbf{R}^T \\ \mathbf{R} (\mathbf{U}_l^P)^T & \mathbf{R} \mathbf{R}^T + \beta^R \mathbf{I} \end{bmatrix}^{-1} \quad (6)$$

where column k of matrix \mathbf{U}_l^a is $\mathbf{u}_l^a(k\Delta t)$, column k of the matrix \mathbf{U}_l^P is $\mathbf{u}_l^P(k\Delta t)$, and β^P and β^R are the adjustable regularization parameters for the physics-based model output and reservoir state output, respectively. The column k of the matrix \mathbf{R} is $\chi(\mathbf{r}(k\Delta t))$, and the reservoir states $\mathbf{r}(k\Delta t)$ for $k = -K + K_T, -K + K_T + 1, \dots, 0$ are obtained by iterating Eq. (1).

For the ML-only oceanic prognostic equations, the solution to the minimization problem for the equivalent of the cost function of Eq. (5) for the ocean is

$$\mathbf{W}'_l = \mathbf{V}^a (\mathbf{R}')^T (\mathbf{R}' (\mathbf{R}')^T + \beta' \mathbf{I})^{-1} \quad (7)$$

where column k of matrix \mathbf{V}^a is $\mathbf{v}_l^a(k\Delta t')$, column k of \mathbf{R}' is $\chi(\mathbf{r}'(k\Delta t'))$, and β' is the Tikhonov regularization parameter.

2.4 Synchronization and Prediction

In order to make a forecast with the trained model from a forecast start time $K_f \Delta t$, we need both the observation-based data and the *synchronized* reservoir states to be available at that time for all sub-domains. The synchronized reservoir state $\mathbf{r}_l(K_f \Delta t)$ at time $K_f \Delta t$ for sub-domain l can be obtained by iterating Eq. (1) using the appropriate observation-based data for times $k\Delta t$ where $k = K_f - K_T, K_f - K_T - 1, K_f - K_T - 2, \dots, K_f - 1$. We allow K_T to be large enough such that, to a high degree of accuracy, $\mathbf{r}_l(K_f \Delta t)$ does not depend on the arbitrary choice of initialization of the reservoir state $\mathbf{r}_l((K_f - K_T)\Delta t)$ (this is what we mean by ‘‘synchronization’’). The reservoir state $\mathbf{r}_l((K_f + 1)\Delta t)$ at time $(K_f + 1)\Delta t$ can then be obtained by using $\mathbf{r}_l(K_f \Delta t)$ and the corresponding observation-based data according to Eq. (1). The property that the reservoir states do not depend on their arbitrary initial choice is called the ‘‘echo state property’’ (Jaeger [2001], Lukoševičius [2012], Lukoševičius and Jaeger [2009]), and we assume that relevant hyperparameters (e.g., the spectral radius, ρ , of \mathbf{A}) of the reservoir are chosen so that the conditions for this property are satisfied. We can then use the appropriate prediction equations (Eq. (2) or Eq. (4)) to make a Δt -step forward prediction. The forecasts of all sub-domains, which can be produced independently and in parallel, are pieced together to create the corresponding global forecast ($\mathbf{u}_G^H((K_f + 1)\Delta t)$ and $\mathbf{v}_G^M((K_f + 1)\Delta t)$) at time $(K_f + 1)\Delta t$ (see Fig. 3). A $2\Delta t$ -step forward prediction can be obtained by advancing the local reservoir states forward using Eq. (1) and by setting $\mathbf{u}_l^{(in)}((K_f + 1)\Delta t)$ or $\mathbf{v}_l^{(in)}((K_f + 1)\Delta t)$ equal to the appropriate sub-vector of the $(K_f + 1)\Delta t$ global forecast vector corresponding to the sub-domain l . The updated reservoir state $\mathbf{r}_l((K_f + 2)\Delta t)$ is then used to make a forecast for time $(K_f + 2)\Delta t$. In this way, we can operate the model in an auto-regressive configuration where the model output at time Δt is fed back in as input to the model when making a forecast for time $2\Delta t$. This allows us to make forecasts of arbitrary lengths into the future.

2.5 Experimental Design and the Choices of the Model Hyperparameters

In the previous description of the ML components, various adjustable parameters were introduced. There are two classes of adjustable parameters. One class is all of the elements of the W -matrices. The values of these parameters are determined by the training procedures we have already described in subsection 2.3. The second class of parameters, called hyperparameters, are not determined by the above-described training procedures. We now briefly discuss the choice of hyperparameters (e.g., d , N , ρ , b , and β for the atmospheric hybrid model component, and d' , N' , ρ' , b' , and β' for the ocean ML-only model component), and we also comment on some of the design choices regarding the ML-only oceanic model component. For the hybrid atmospheric model component, we use the same hyperparameters

as described in AEA23. For the oceanic model component, we use the same hyperparameters for reservoir computers across all sub-domains. We found that, for example, varying the spectral radius with latitude in a fashion similar to that for the atmospheric model component does not improve the ability of the oceanic model component to predict SSTs. Each sub-domain is modeled by a reservoir computer of $N' = 6000$ nodes, with a reservoir adjacency matrix of nodal degree $d' = 6$ and spectral radius of $\rho' = 0.9$, an input matrix with an input coupling strength of $b' = 0.6$, and a Tikhonov regularization parameter of $\beta' = 100$. We found that using a reservoir with a larger N' did not significantly improve the forecast skill of the model. Furthermore, we found that the skill of the oceanic model component was not very sensitive to the choice of d' , ρ' (for $0.3 < \rho' < 0.9$), and b' (for $0.3 < b' < 1.4$). On the other hand, we found that the model's skill was more sensitive to the Tikhonov regularization strength (which we tested in powers of 10 from 10^{-4} to 10^3), and the leaking rate parameters c'_i for $i = 1, \dots, N'$. In fact, for Tikhonov regularization strengths lower than 1, we found that the model was significantly more likely to become unstable during prediction. We selected the leaking rate for each reservoir node by randomly choosing values from a log-uniform distribution over the interval $[10^{-3}, 1]$ like Tanaka et al. [2022]. We found that using multiple leaking rate values (i.e., as opposed to choosing a single leaking rate $c'_i = c$ for a constant c for all reservoir nodes) was crucial to allowing the ocean model to simultaneously predict both the SST and the 300 m oceanic heat content fields with realistic multi-year variability.

The inclusion of 300 m ocean heat content as a prognostic variable in the oceanic model component was motivated by physical reasoning, e.g., that the knowledge of the upper-oceanic heat content can improve predictions of the El Niño cycle, especially across the so-called “spring predictability barrier” (McPhaden [2003], Ji and Leetmaa [1997], Clarke and Van Gorder [2003]). As expected, this modification noticeably improved the overall forecast performance of the model, including an extension of the skill of the model to predict the El Niño cycle by at least 2 months. For similar reasons, we also tried adding the ocean mixed layer depth as a prognostic variable to the model, but found that it did not improve the performance of the model. We did tests (only cursory, however, due to computational constraints) of the effects of including only some atmospheric variables of the lowest atmospheric model level in the input to the ocean model. We added, one-by-one, the temperature, the two components of the horizontal wind vector, and the specific humidity of the lowest atmospheric model level, and (the natural logarithm of) the surface pressure. We found that the addition of each variable contributed to obtaining realistic temporal variability and/or extending the forecast horizon of the model-predicted SSTs. In addition, we tried inputting a signal that consisted of the sine and cosine of the day of the year multiplied by $2\pi/365$ to the ocean (and atmospheric) model in order to encode knowledge of the time of the year. This did not, however, appear to provide any performance benefits. The time step $\Delta t'$ for the ocean model is also a hyperparameter and we tested time steps of 1-day, 3-days, 7-days, and 1-month. We found that the 3-day time step resulted in the best overall model performance. While the 7-days and 1-month time steps also produced good results, the 1-day time step resulted in noticeably degraded performance (possibly due to the choice of other hyperparameters). Some of our other tests included having an input-pass-through (i.e., the input to the reservoir is also provided as an input directly to the output layer), training to predict tendencies rather than the state itself (i.e., $\delta\mathbf{x}(t + \Delta t) = \mathbf{x}(t + \Delta t) - \mathbf{x}(t)$ instead of $\mathbf{x}(t + \Delta t)$), and separate Tikhonov regularization strengths for the input-pass-through component and the reservoir state component of the output feature vector. None of these methods appeared to improve the model performance (and in some cases they degraded it), and were therefore left out of the final version of our model.

3 Data

The global analyses for the atmospheric variables and SST are hourly ERA5 reanalyses (Hersbach et al. [2020]) interpolated spatially to the SPEEDY computational grid using a 2-dimensional quadratic B-spline interpolation in the horizontal direction and a 1-dimensional cubic B-spline interpolation in the vertical direction (to fit to the eight prescribed constant values of σ). The global analyses for the 300 m oceanic heat content are the monthly mean ORAS5 reanalyses (Zuo et al. [2019]) interpolated spatially to the SPEEDY computation grid as described for the ERA5 reanalyses. In addition, the ORAS5 data is linearly interpolated to hourly data in the temporal domain. The training starts at 0000 UTC on 1 January 1981 and ends at 0000 UTC on 27 December 2002 ($K \approx 1.93 \times 10^5$).

4 Results

In this section we assess the forecast skill of our trained model. The results presented below are based on 195 2-year long forecasts, with start times equally spaced by 30 days between 0000 UTC 16 January 2003 and 0000 UTC 23 December 2018. We evaluate the forecast performance of our model by comparing against ERA5 data for the corresponding dates. When appropriate, we also include the performance metrics for the persistence and climatology based forecasts for comparison. By persistence based forecast, we mean using the observational analysis that serves as the initial condition of the forecast to provide the forecast for the entire forecast time, that is, keeping the forecast state constant in time.

The climatology based forecast uses the climatological values of the prognostic state variables for the specific location and calendar time of the year.

We compare the Pearson correlation coefficient (PCC) and the root-mean-square error (RMSE) of scalar state component time series between our model predictions and the corresponding ERA5 observation-based data as a function of prediction lead time. In Sec. 4.1, we explain how we compute these metrics. For cases where we show these metrics on a spatial map, we obtain those results by applying the methods described in Sec. 4.1 at each spatial grid point independently. Letting t denote the prediction lead time in Sec. 4.1, we use $\{x_i(t)\}_{i=1,2,\dots,N_T}$ for a collection of N_T predicted uni-variate time series and $\{y_i(t)\}_{i=1,2,\dots,N_T}$ for the corresponding collection of N_T “ground truth” uni-variate time series.

4.1 Forecast Verification Metrics

4.1.1 Pearson Correlation Coefficient

The Pearson correlation coefficient as a function of prediction lead time t is given by

$$r(t) = \frac{\sum_{i \in S} (x_i(t) - \bar{x}(t))(y_i(t) - \bar{y}(t))}{\sqrt{\sum_{i \in S} (x_i(t) - \bar{x}(t))^2 (y_i(t) - \bar{y}(t))^2}}, \quad (8)$$

where S is the set of indices denoting the forecasts used when computing the PCC (e.g., we may only include forecasts with start dates in the month of June when assessing the forecast skill of the model for the June-July-August season). The over-bar ($\bar{(*)}$) denotes the average of $(*)_i$ for $i \in S$. When considering the ability of a model to predict an anomaly signal, it is a common practice in the literature to accept as a valid forecast horizon the maximum prediction lead time for which the PCC is greater than or equal to 0.5 (i.e., $\max\{t | r(t) \geq 0.5\}$) (Owens and Hewson [2018], Ham et al. [2019], Zhou and Zhang [2023]). We follow this convention as one of our metrics to assess forecast skill. We also calculate the 95% confidence interval associated with our PCC values to estimate their statistical significance.

4.1.2 Root-Mean-Square Error

The root-mean-square error as a function of lead time t averaged over a collection of univariate time series is given by

$$RMSE(t) = \sqrt{\frac{\sum_{i \in S} (x_i(t) - y_i(t))^2}{|S|}} \quad (9)$$

where $|S|$ denotes the number of elements in S . When appropriate, we also report the RMSE for the persistence and climatology based forecast. The relationship between model forecast errors and those of the persistence and climatology is well understood, (e.g., Section 3.8 of Szunyogh [2014]). The RMSE of the persistence based forecast, while smaller than the RMSE of the climatology based forecast at shorter lead times, saturates at a value $\sqrt{2}$ times greater than the climatology error at longer lead times. If our model has useful short-term forecast skill, we can expect it to produce forecasts with a lower value of the RMSE than that of the persistence based forecasts. If our model has realistic climatology, then the RMSE of the forecasts at longer lead times should saturate at the same level as that for the persistence based forecasts.

4.2 El Niño Cycle and its Teleconnections

The El Niño cycle is the dominant driver of year-to-year global climate variability (McPhaden et al. [2006], Lin and Qian [2019], Timmermann et al. [2018]). It is a coupled ocean-atmosphere climate phenomenon (Bjerknes [1969]) with three phases, which are characterized by the presence of anomalously warm (El Niño), anomalously cool (La Niña), or normal (neutral) sea surface temperatures in the central and eastern tropical Pacific Ocean. El Niño or La Niña conditions are usually accompanied by anomalous atmospheric weather patterns across the globe, e.g., increased/decreased rainfall (Lin and Qian [2019], Wang et al. [2013], Losada et al. [2012], Dai and Wigley [2000]), and predicting the El Niño cycle holds significant socioeconomic and environmental value (Liu et al. [2023]). Below we describe our model’s skill in predicting this phenomenon and some of the teleconnections associated with it (Alexander et al. [2002]).

The phase of the El Niño cycle is often characterized by monitoring a uni-variate time series of the spatially-averaged monthly mean SST anomalies in the Nino 3.4 (5°N-5°S, 170°W-120°W), Nino 3 (5°N-5°S, 150°W-90°W), or Nino 4 (5°N-5°S, 160°E-150°W) region. These three indices are also often used to categorize El Niño events into types, e.g., Eastern-Pacific and Central-Pacific (Ashok et al. [2007]). Figure 4 shows our model’s forecast skill for predicting these three El Niño signals according to the PCC (blue curves) and RMSE (red curves) metrics. Figures 4(a-c) show the all-season forecast skill as a function of prediction lead time and Figs. 4(d-f) show the PCC of our model forecasts as a

function of prediction lead time and prediction start date. Figures 4(a-c) also include the performance of the persistence model for this task. The all-season valid forecast horizon of our trained model, i.e., the prediction lead time at which the PCC of our model forecasts against the ERA5 data drops to 0.5 for the first time, is approximately 6 months according to all three Nino indices. While this shows a significant improvement compared to the persistence model for the Nino 3.4 and Nino 3 indices, it is comparable to the skill of the persistence model for predicting the Nino 4 index. We also note that the RMSE of our model forecasts (for all three indices), while lower than that of the persistence model at short prediction lead times, grows larger than that of the persistence model at longer lead times. This indicates that while the version of the model described in the present paper has more skill predicting the weather even beyond the medium forecast range than that of AEA23, it is less appropriate for long-term climate simulations, because the AEA23 version of the model produced more realistic El Niño cycles in a 70 year long climate simulation. As a function of prediction start month, the valid forecast horizon of our model (for all three indices) ranges from about 4 months for forecasts initiated in the spring to about 8 months for forecasts initiated in the summer. The low predictability of El Niño for forecasts initiated in the spring can be attributed to the “spring predictability barrier” (Zheng and Zhu [2010], Lai et al. [2018]).

Broadly speaking, there are two classes of forecasting models to which we can compare the results of our hybrid model. The first consist of purely physics-based models, e.g., the coupled models from the North American Multi-Model Ensemble (NMME) which have valid forecast horizons ranging from 7-9 months when tested over the 1983 – 2010 period (see Fig. S6 in the Supplemental Materials of Zhou and Zhang [2023]). Based on this published result and our results presented in Fig. 4, our hybrid model has useful skill in forecasting El Niño that is comparable that of the members of the NMME. This comparable performance is achieved while requiring substantially more modest computing resources to generate forecasts. We note that, once trained, the majority of the computing cost of our hybrid model can be attributed to frequently restarting the knowledge-based component (SPEEDY), which is a low-resolution AGCM. Evidently, despite using a low-resolution AGCM as the knowledge-based component of our hybrid model (which is computationally cheaper to operate than high-resolution coupled models like those used in NMME) we are able to obtain results comparable to computationally more expensive physics-based models. The second class of forecasting models we can compare our results to are purely data-driven models such as machine learning models (Ham et al. [2019], Zhou and Zhang [2023]). While such models are better at predicting the ENSO indices, to the best of our knowledge, they are highly-specialized models that are either directly trained to predict the El Niño indices, or only provide spatiotemporal forecasts in a small geographical region (e.g., the equatorial Pacific Ocean). Furthermore, while such data-driven models typically have a temporal resolution of one month, our ocean component model is an auto-regressive global forecasting model with a time step of 72 hours. Despite having a temporal resolution much finer than the time scale over which El Niño evolves (on the order of months), our model has useful El Niño forecasting skill.

ENSO influences global circulation and weather patterns beyond the medium forecast range via teleconnections (Alexander et al. [2002], Lin and Qian [2019]). For instance, El Niño (La Niña) is typically accompanied by drier (wetter) conditions in the eastern Pacific and over the maritime continent, while ushering wetter (drier) conditions over the southern United States (Ropelewski and Halpert [1987], Mason and Goddard [2001]). The atmospheric response during El Niño events also influences, via the “atmospheric bridge”, ocean basins across the globe (Alexander et al. [2002]). To assess whether our model is able to capture the global effects of this phenomenon at the seasonal time scale, we investigate the ability of our model to capture the observed seasonal correlations between El Niño and other variables, e.g., SSTs and precipitation, across the globe.

To this end, in Fig. 5 we examine the all-season correlations between the 3-monthly-averaged SST anomalies at each grid point and the Nino 3.4 Index. Specifically, the top row of Fig. 5 shows concurrent correlations where the SST anomalies and the Nino 3.4 Index are evaluated at the same times. For the lagged correlations shown in the bottom row, we use the Nino 3.4 Index for a given 3-month period (i.e., DJF, MAM, JJA, or SON) and the 3-monthly averaged SST anomalies at each grid point for the following season. Panels in the left and right columns of Fig. 5 show the correlations between the SST anomalies and Nino 3.4 Index predicted by our model, and between those quantities obtained from ERA5 data, respectively. We see that our model predictions capture the observed strong positive correlations between the Nino 3.4 Index and SSTs stretching from the central and eastern equatorial Pacific Ocean up (down) to the western coast of North (South) America. In addition, our hybrid model captures the “horseshoe” shaped negative correlations in equatorial western Pacific, northwestern Pacific and southwestern Pacific. We also see that our model captures the strong positive correlations in the Indian Ocean. We note, however, that in the lagged correlations our model somewhat overemphasizes the positive correlations in the central Atlantic and the negative correlations in the northwestern Pacific. We also see that our model is slightly under-emphasizing the spatial extent of the positive correlations off the western coast of North America. Despite these small difference, we find that our model is able to capture the general large-scale correlations between SST anomalies in the tropical Pacific and in the rest of the oceans, which is a key component in the El Niño teleconnections (Alexander et al. [2002], Lin and Qian [2019], Roy et al. [2019]).

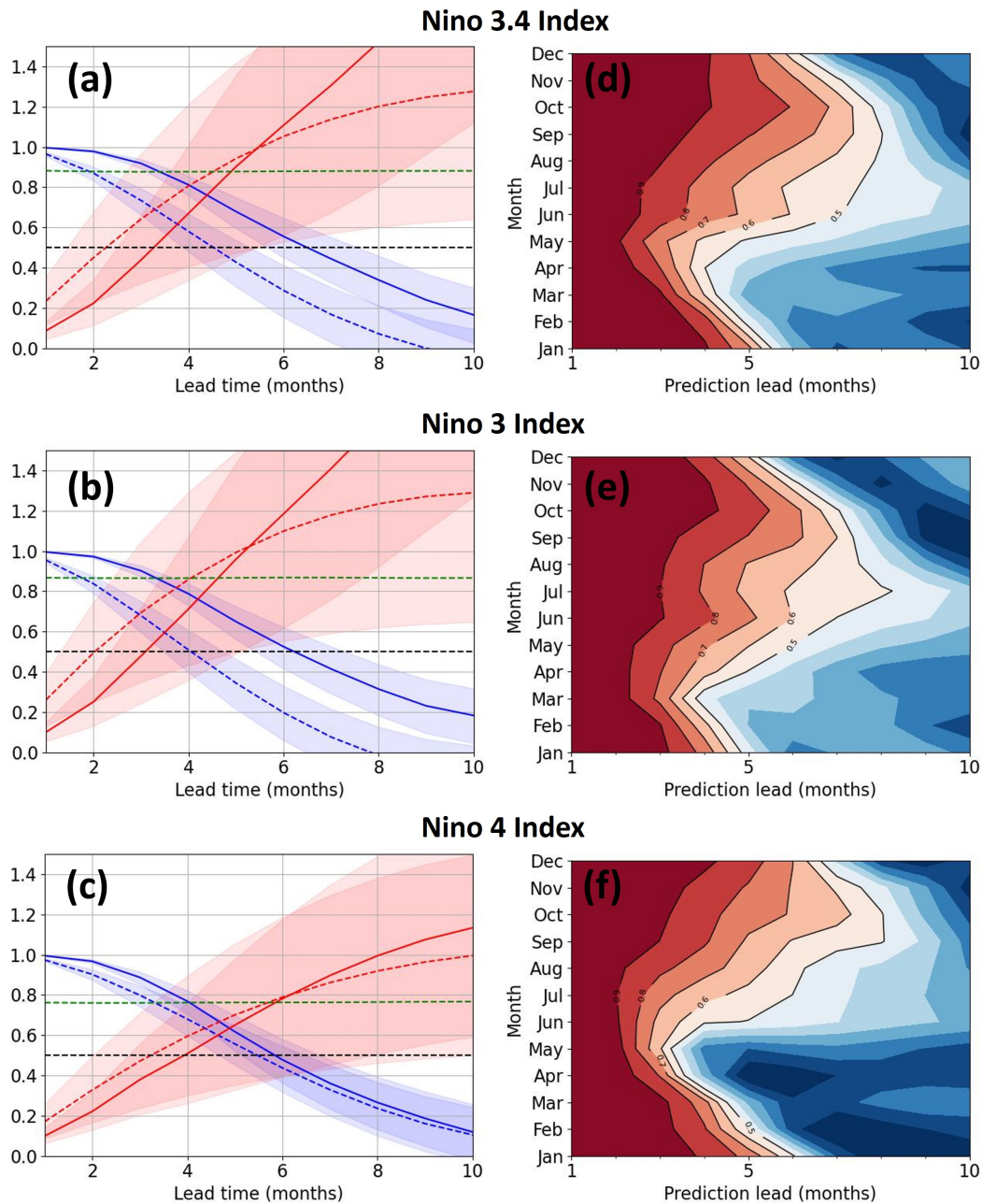


Figure 4: The all-season Pearson correlation coefficients and root-mean-square errors between the predicted and observation-based Nino 3.4 Index (a), Nino 3 Index (b), and Nino 4 Index (c) as a function of lead time in months. Solid (dashed) blue curves show the PCC for our model's (persistence model's) predictions. Dashed green curve shows the RMSE for the climatology model's predictions. Solid (dashed) red curves show the RMSE for our model's (persistence model's) predictions. (d), (e), and (f) show the PCC for our model's prediction as a function of the prediction lead time (in months) and the prediction start month for Nino 3.4 Index, Nino 3 Index, and Nino 4 Index, respectively.

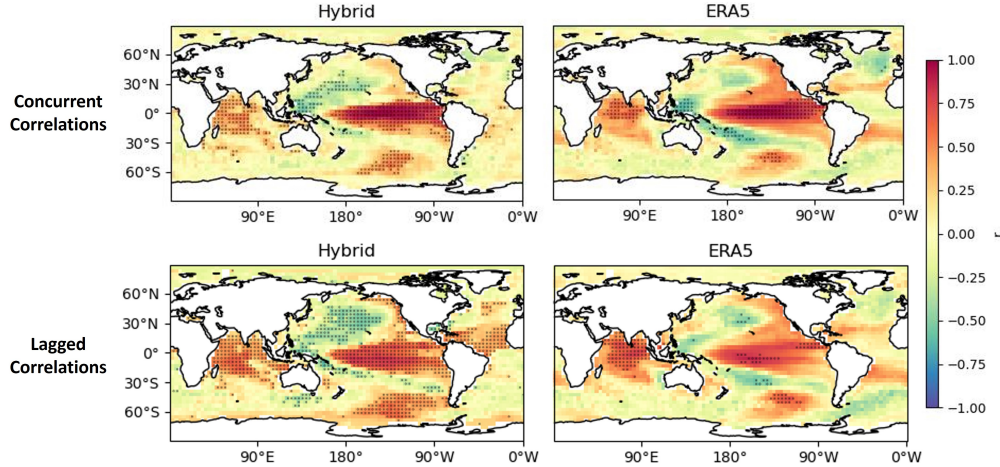


Figure 5: The top row shows the all-season concurrent PCC between the Niño 3.4 Index and the 3-monthly averaged SST anomalies. The bottom row shows the all-season lagged PCC between the Niño 3.4 Index and the lagged 3-monthly averaged SST anomalies. The left column (with panels titled “Hybrid”) shows the correlation between the predicted Niño 3.4 Index and predicted SST anomaly values and the right column (with panels titled “ERA5”) shows it for observation-based data. Black dots indicate grid points for which the PCC was found to be statistically significant at the 95% confidence level.

In the left column of Fig. 6, we plot the concurrent correlations between the predicted 3-monthly-averaged precipitation anomalies at each grid point and the predicted Niño 3.4 Index for each season, both at a prediction lead time of 1 season. The right column shows similar plots for the precipitation anomalies and Niño 3.4 Index obtained from the ERA5 data. The rows correspond to the DJF, MAM, JJA, and SON seasons, from top to bottom in that order. To calculate the correlations for our model predictions for DJF, for example, we use the predicted DJF-averaged precipitation anomalies from all forecasts beginning in December and the Niño 3.4 Index values corresponding to those DJF periods. (Note, while each of our forecasts is 2 years in length, we only use the forecasts for the 3 months following the start of the forecast.) In addition, we placed a black dot on each grid point for which the calculated correlation value was found to be statistically significant at the 95% confidence level. El Niño activity peaks in the DJF period and we see the resulting strong El Niño-precipitation correlations in the “DJF: ERA5” panel of Fig. 6, which shows the global correlation patterns between the observed precipitation anomalies and Niño 3.4 Index for this period. As seen in the “DJF: Hybrid” panel of Fig. 6 (and by comparing to the corresponding correlations obtained from ERA5 data), we see that, e.g., our trained model captures the strong positive correlations between the tropical Pacific SST anomalies and precipitation anomalies in the central/eastern Pacific Ocean, northeastern Pacific Ocean, western Atlantic Ocean along the United States, and over the central Indian Ocean. Similarly, our model captures the strong negative correlations between the tropical Pacific SST anomalies and precipitation anomalies over the maritime continent, the Pacific Ocean to the north and south of the Niño 3.4 region, and over the northeastern South America. While our model over-emphasizes the strength of some of these correlations, e.g., the positive correlation over the western Atlantic Ocean along the eastern United States, it generally captures the correct sign of the correlation with statistical significance at a 95% confidence level and has realistic spatial patterns for the correlations. We note, however, that our model struggles in some regions, e.g., it incorrectly predicts strong positive correlations over the Arabian peninsula and northern Indian sub-continent during the DJF period. It also struggles to capture the strong negative correlations between summer monsoon activity over the Indian sub-continent and the maritime continent, and the Niño 3.4 Index. Overall, however, we find from inspecting these figures that our model forecasts generally contain El Niño-precipitation correlation patterns that resemble those observed in the ERA5 data set, particularly over regions where significantly strong positive or negative correlations exist.

4.3 Global Precipitation

An important task for models that forecast weather beyond the medium range is to correctly predict precipitation anomalies at lead times ranging from several days to several weeks. Next, we investigate whether our model has useful skill for this task. We do so by using the PCC between the ERA5-based precipitation anomalies and those predicted by our model. We note that such PCC is a commonly used deterministic verification metric for this task (de Andrade et al. [2019], Li and Robertson [2015], Zhao et al. [2019]). It is also important to emphasize that even though each ERA5

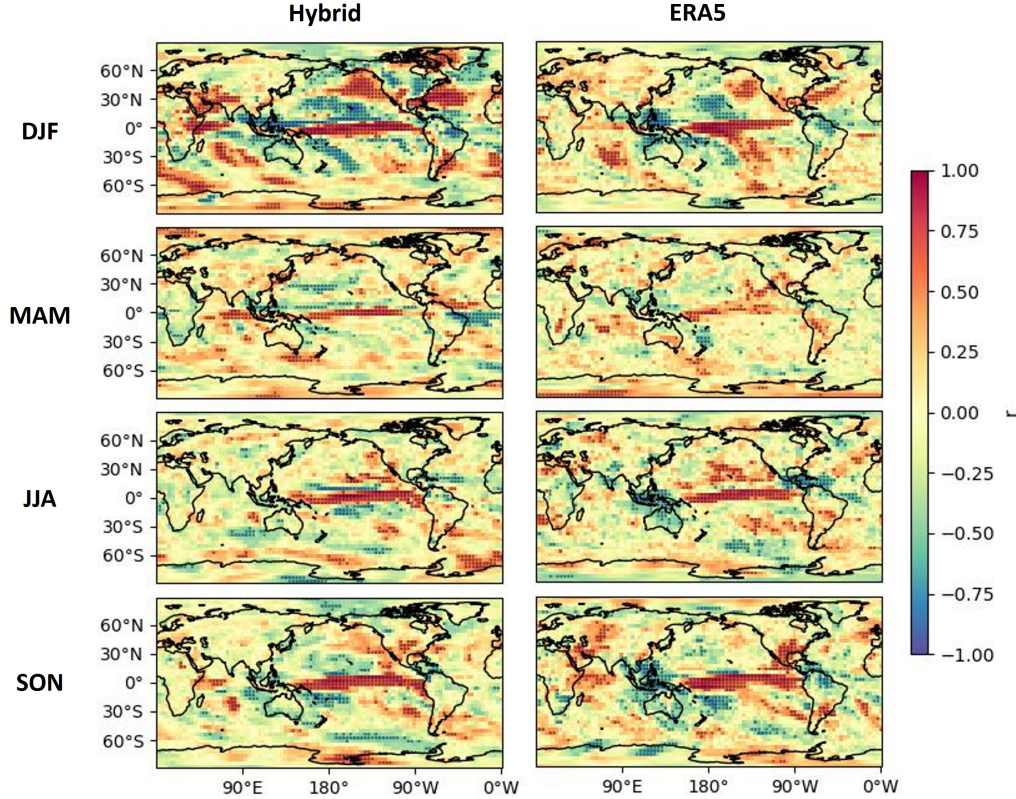


Figure 6: The left (right) column, with the label “Hybrid” (“ERA5”) shows the Pearson correlation coefficients between the precipitation anomalies and the Niño 3.4 Index predicted by our model (obtained from ERA5 data) at a prediction lead time of 1 season. The rows, in order from the top-most to the bottom-most, correspond to results for the December-January-February (DJF), March-April-May (MAM), June-July-August (JJA), and September-October-November (SON) seasons. Black dots indicate grid points for which the PCC was found to be statistically significant at the 95% confidence level.

analysis is based on millions of observations, these observations do not include precipitation observations for most of the globe. The only exceptions are composite ground-based radar/rain-gauge precipitation estimates over the United States east of the Rockies from 2009 onward (Hersbach et al. [2020]). Thus the ERA5 precipitation analyses primarily reflect the precipitation response of the ECMWF Integrated Forecasting System (IFS) Cy41r2 conventional model, which was used in ERA5 to obtain the background fields, to the assimilation of the observations of other state variables. The ERA5 precipitation analyses have the largest errors in the tropics (e.g., Lavers et al. [2022]). But, because the precipitation prognostic variable of our model was trained on ERA5 precipitation data, the precipitation diagnostics presented here are good measures of the skill of the proposed modeling approach to learn from precipitation training data.

Figure 7 shows the all-season spatial correlations between the weekly-mean precipitation anomalies in our model forecasts and the ERA5 data. We see that our model has strong positive correlations across much of the globe at a lead time of 1 week, and that these correlations decay rapidly afterwards. Strong positive correlations persist mostly near the tropics out to a lead time of 4 weeks. The spatial correlation patterns in our results share similar features to those obtained from some of the models in the S2S prediction project (e.g., Figure 1 in de Andrade et al. [2019] as well as results in Li and Robertson [2015] and Zhao et al. [2019]). There are regions where our model struggles even at a lead time of 1 week, e.g., over central and western Africa and western South America, but we note that these appear to be similarly problematic regions for many state-of-the-art models, including those in the S2S prediction project (de Andrade et al. [2019]). Overall, our model appears to have useful skill comparable to conventional models (de Andrade et al. [2019]) in predicting weekly global precipitation anomalies at sub-seasonal time scale and we find that the skill decays rapidly with lead time in a way similar to what is found for the operational prediction models.

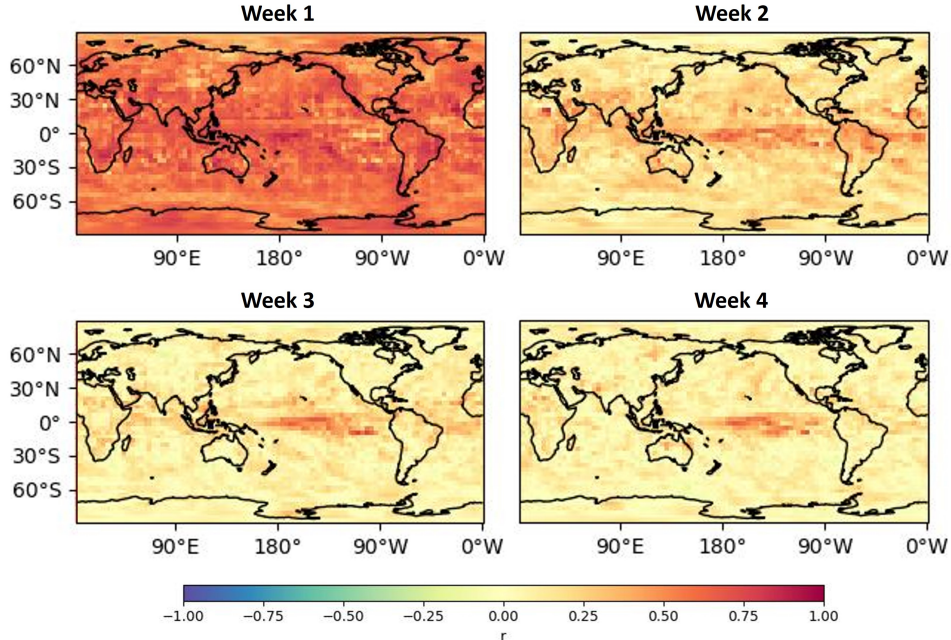


Figure 7: The Pearson correlation coefficients between the precipitation anomalies in the model forecasts and the ERA5 data at forecast lead times (from left to right) 1, 2, 3, and 4 weeks.

Rainfall anomalies in the tropical Pacific can impact weather and climate across the globe, making the prediction of tropical rainfall an important task for models. Current models suffer from substantial biases in this region (Lee et al. [2022], Sobel et al. [2023], You et al. [2024]). To evaluate the skill of our model in predicting rainfall in the tropical Pacific, we calculate verification metrics for two geographical regions: the East Pacific ($15^{\circ}S - 15^{\circ}N$, $180^{\circ}W - 130^{\circ}W$), and the West Pacific ($15^{\circ}S - 15^{\circ}N$, $130^{\circ}E - 180^{\circ}E$). You et al. [2024] suggested separating these two regions and our verification results (Fig. 8 and Fig. 9) also confirm that they pose different challenges. These results are for the prediction of precipitation anomalies, which are calculated as follows. We first obtain the daily accumulated precipitation anomalies for both our forecasts and ERA5 by subtracting the corresponding ERA5 based day-of-the-year accumulated precipitation climatological mean. Next, for each day in the forecast (and the corresponding verification ERA5 data), we calculate a trailing 5-day sum of the accumulated precipitation anomalies. Finally, we perform a spatial average over the region of interest to obtain a uni-variate time series of the pentad accumulated precipitation anomalies. Panel (a) of both figures shows the PCC as a function of lead time for our model forecasts and the forecasts based on persistence. In the East Pacific region, the PCC initially (for the first pentad) is higher than 0.5, and as the forecast lead time increases, it converges to about 0.5 for both forecasts. The result that the PCC converges to 0.5 rather than zero indicates that in this region the anomalies typically have a component that changes at time scales that are substantially longer than the longest (19 days) lead time in the figures. Nevertheless, our model predicts the part of the anomalies that affects the forecast accuracy in the investigated range more accurately than persistence for about 15 days. Predicting the anomalies is more challenging in the West Pacific, where the PCC for the persistence based forecast is already lower than 0.5 at initial time, and it drops to zero by 10 days lead time, showing that the anomalies change fast in this region. Our model does well in predicting these anomalies, greatly outperforming the persistence based forecasts. The PCC drops to 0.5 at about 12.5 days lead time and it does not yet reach zero even at 18 days lead time. Panels (b-e) show scatter plots of the predicted (horizontal axis) and ERA5-based (vertical axis) precipitation anomaly values used for the calculation of the PCC. These plots suggest that the anomalies tend to have positive values more often than negative values. This can be explained by a shift in the distribution of spatially-averaged pentad accumulated precipitation values in ERA5 that occurs around 2002 (not shown here). For example, the ERA5 average pentad accumulated precipitation (spatially-averaged over the WP region) appears to have increased by about 9% for the time period of 2003 – 2020 from its average value over the time period of 1981 – 2002. We used the ERA5 data corresponding to the period 1981 – 2002 (i.e., the data used for training our model) to calculate the day-of-the-year precipitation climatological means which were subsequently used to calculate the anomalies for the verification period (2003 – 2020).

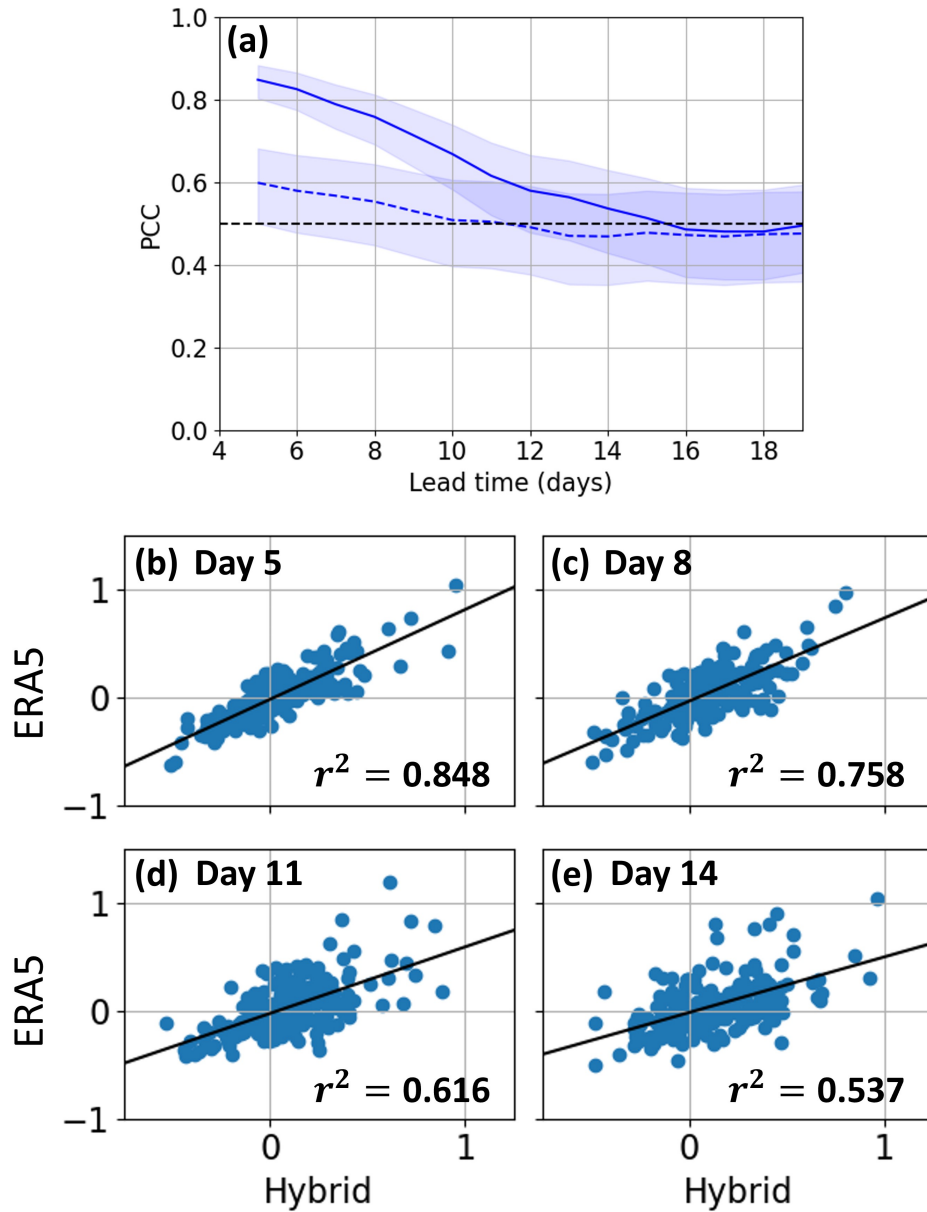


Figure 8: Precipitation forecast verification results for the Tropical East Pacific. Shown is (a) the PCC versus forecast lead time for (solid blue) our model forecasts and (dashed blue) the persistence-based forecasts. The black dashes indicate PCC=0.5. Also shown are scatter plots of the spatially-averaged pentad accumulated precipitation anomalies for (horizontal axis) our model predictions and (vertical axis) the ERA5 data at forecast lead times (b) 5, (c) 8, (d) 11, and 14 days, respectively.

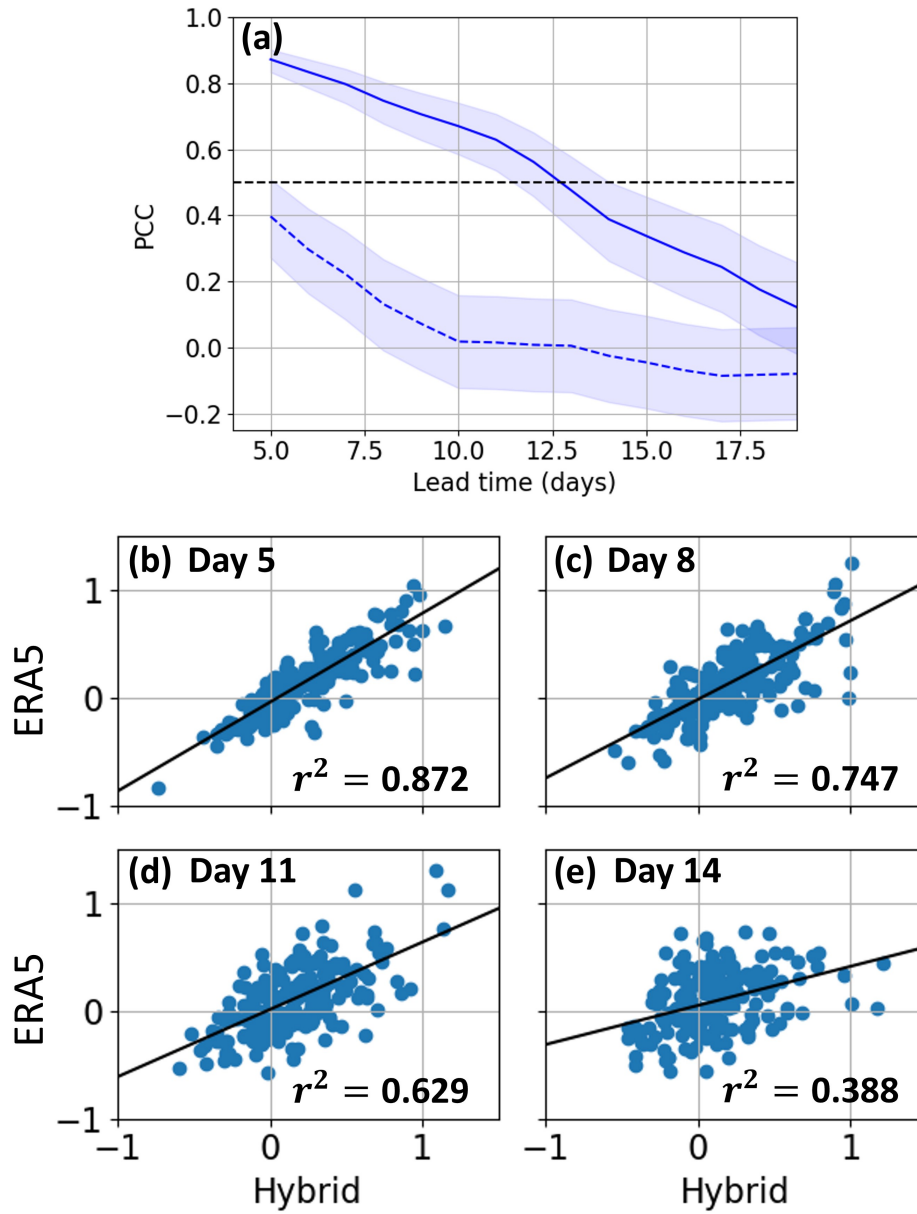


Figure 9: Same as Figure 8, except for the Tropical West Pacific.

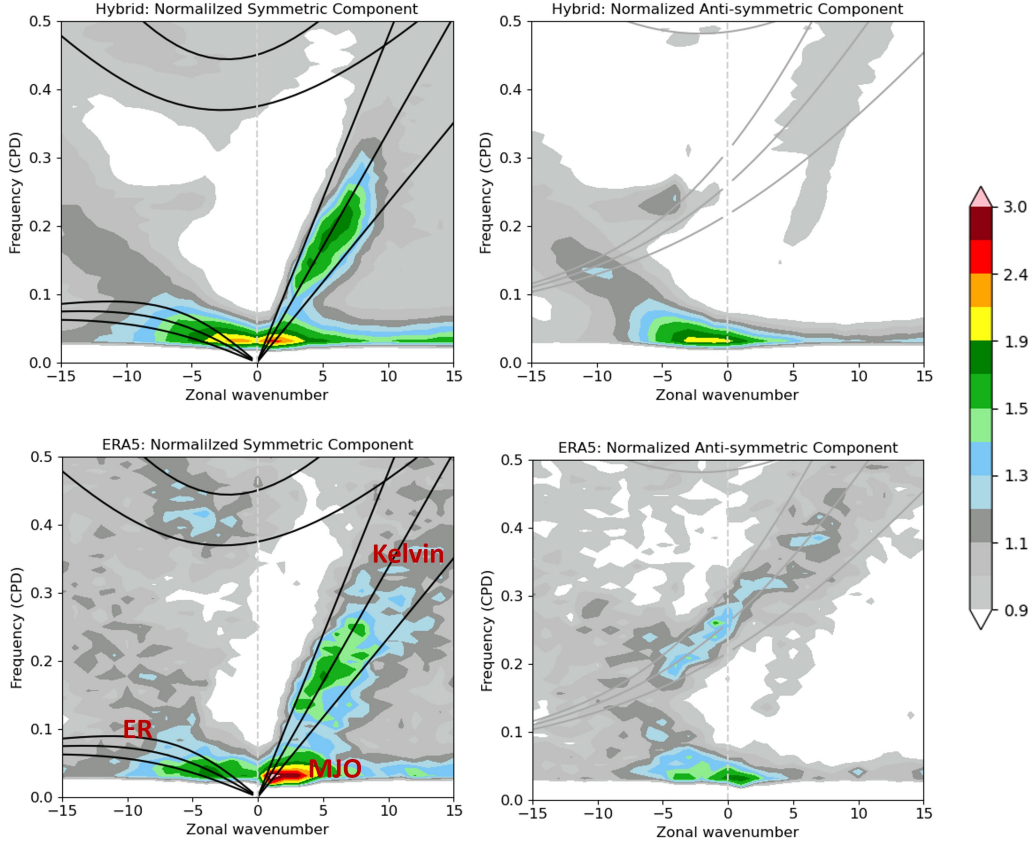


Figure 10: The top (bottom) row shows the Wheeler-Kiladis diagram obtained by using the precipitation in the 15°S - 15°N latitude band predicted by our model (obtained from ERA5 data). The left (right) column shows the normalized symmetric (anti-symmetric) components of the wavenumber-frequency analysis. The horizontal axis of each plot represents the zonal wavenumber and the vertical axis represents the frequency (cycles per day). The solid black lines indicate solutions to the dispersion relations from an analytical model of shallow water waves.

4.4 Convection-Coupled Equatorial Waves

Convection-coupled equatorial waves organize convective cells into “synoptic scale” traveling disturbances in the tropics. Maintaining these waves in longer range model forecasts is important, because they are thought to play an important role in predictability through teleconnections. With the exception of the MJO, these waves are equatorially trapped wave solutions of the shallow-water equations on a beta-plane (Matsuno [1966] and Lindzen [1967]). A Wheeler-Kiladis diagram (Wheeler and Kiladis [1999]), obtained by performing a space-time spectral analysis, has become a standard tool for the detection of convection-coupled equatorial waves in observed, analyzed, and model simulated or forecast fields of atmospheric state variables. It uses the dispersion relations of the waves as predicted by shallow-water theory, as well as the phenomenology based spectral characteristics of the MJO, to detect the waves in data.

Figure 10 shows Wheeler-Kiladis diagrams for the 6 h cumulative precipitation in the 15°S - 15°N latitude band. The top row shows results for our model based on the 2-year long forecasts, while the bottom row shows the related diagrams for the ERA5 data. The results show that our model captures the enhanced variability of the precipitation associated with Kelvin waves and equatorial Rossby (ER) waves. While our model has slightly lower spectral power in the MJO region (in the lower positive zonal wave numbers and at lower frequencies), it has a power distribution similar to observations for “synoptic-scale” disturbances at low frequencies wave numbers. In comparison, various conventional purely physics-based models, such as E3SM and CFSv2 (see, e.g., Goswami et al. [2017], and Golaz et al. [2022]), struggle to capture these equatorial waves. Overall, we see that the tropical precipitation spectral power distribution from our trained model matches well in many regimes with observations, indicating that our model has learned a realistic representation of tropical convective processes.

5 Conclusions and Outlook

In this paper, we explored the potential of a hybrid modeling approach for weather prediction beyond the medium forecast range. We made several modifications to the previous (AEA23) version of our prototype hybrid model that implements this approach to further improve its forecast performance in this extended range. These modifications included adding a new ML-based internal prognostic variable to the oceanic component of the model for the heat content of the top 300 m layer of the ocean. Other modifications were made to the dynamics of the reservoir computing units of the ML-based oceanic model component to better handle the disparate time scales of the oceanic and atmospheric dynamics. The results of our forecast experiments showed that our model has useful forecast skill, similar to that of much higher resolution conventional purely physics-based models, for various oceanic and atmospheric phenomena that play important roles in predictability in the investigated forecast ranges. These phenomena include the El Niño cycle and some of its extratropical teleconnections, and the signatures of convection-coupled equatorial waves in the precipitation fields. In particular, our model makes predictions of the El Niño cycle that are similar in skill to those with the operational S2S prediction systems; it captures the strongest teleconnections patterns between El Niño and the precipitation patterns around the world; and it is able to capture Kelvin wave and equatorial Rossby wave activity in 2-years long forecasts. We have obtained such results with a hybrid model that requires fewer computing resources than the substantially higher resolution, currently operational, traditional physics-based models.

The forecast performance of the model could most likely be further improved with the addition of more ML-based prognostic variables to better capture the two-way interactions between the atmosphere and components of the Earth system other than just the ocean, such as land and the cryosphere. Also, because the cumulative precipitation variable is purely ML-based, it could be trained on a processed observational product such as NASA’s Integrated Multi-satellite Retrievals for GPM (IMERG) data set rather than ERA5 reanalyses. This variable could even have higher spatial resolution than the other prognostic variables. These two changes could greatly increase the quality of the precipitation forecasts.

We believe that the forecast skill of our model in terms of root-mean-square error could be substantially increased by replacing our single-initial-condition deterministic forecasts with the mean of an ensemble of model forecasts. In fact, the ensemble approach is the standard operational approach to make model predictions beyond the medium range. Ensemble averaging minimizes the forecast RMSE by filtering uncertain details from the forecasts. As the forecast lead time increases, the ensemble mean converges to climatology (Epstein [1969], Leith [1974]). At intermediate lead times, if the ensemble is initialized appropriately, the ensemble mean provides an optimal blend of the initial condition-dependent and the climatology-based information in the least-square sense. Because ML-based models also optimize forecasts in the least-square sense, an ML-based model solution with time step Δt can be expected to resemble an ensemble-mean forecast at forecast lead time Δt . Hence, a forecast with our hybrid model is similar to a forecast that has been pieced together from ensemble mean forecasts of length Δt for the atmosphere and length $\Delta t'$ for the ocean. We could increase the time steps to minimize the root-mean-square errors at specific long forecast lead times, but that would lead to the loss of details at the shorter lead times. We speculate that the currently used time steps combined with the ensemble approach would provide a good balance between details and longer term performance.

We see two potential areas for the application of our hybrid modeling approach. First, it could be used for the hybridization of current operational models. Such a hybridization would have the potential to lead to substantial forecast improvements, which could otherwise, at best, be achieved only by years of incremental improvements of the purely physics-based models. Second, a hybrid model based on a low-resolution research AGCM like ours can be a powerful tool of academic research. The computing challenges involved are not overwhelming for a small academic research group in which the hands-on code development is primarily done by graduate research assistants.

As a final comment, our results suggest the important point that the hybrid ML/physics-based modeling approach is potentially capable of skillfully modeling climatological phenomena whose spatial scales can be resolved at the resolution of the hybrid model (Figs. 4-10; see also Figs. 2 and 3 of AEA23). We note that this need not be the case for conventional physics-based models which typically employ subgrid scale modeling whose accuracy strongly affects the behavior of scales resolved by the model, and can be problematic, especially for a low resolution model. In the hybrid approach, however, the training implicitly includes the effects of unresolved scales on the resolved scales, because the training data, although itself essentially at the resolved scales, includes the real effects of the unresolved smaller scale dynamics in determining the observed larger scale dynamics that is being learned (this point has been previously emphasized by Wikner et al. [2020]).

Open Research

The code to run and analyze the results of the experiments in this study are available online (<https://github.com/dhruvitpatel/Hybrid-Weather-Beyond-Medium-Range.git>). The trained weights for the hybrid

model used in this study will be made available online (<https://doi.org/10.5281/zenodo.11390866>). The (results) data needed to perform the analysis shown in the paper will be made available online in the near future.

Acknowledgments

The work of Istvan Szunyogh, Brian Hunt, and Edward Ott on this research was partly supported by the Office of Naval Research under grant N00014-22-1-2319. Portions of this research were conducted with the advanced computing resources provided by Texas A& M High Performance Research Computing. Troy Arcomano was partly supported by the Global Change Fellowship in the Environmental Science Division at Argonne National Laboratory (grant no. LDRD 2023-0236).

References

- Michael A. Alexander, Ileana Bladé, Matthew Newman, John R. Lanzante, Ngar-Cheung Lau, and James D. Scott. The atmospheric bridge: The influence of enso teleconnections on air–sea interaction over the global oceans. *Journal of Climate*, 15(16):2205 – 2231, 2002. doi:10.1175/1520-0442(2002)015<2205:TABTIO>2.0.CO;2.
- Troy Arcomano, Istvan Szunyogh, Alexander Wikner, Jaideep Pathak, Brian R. Hunt, and Edward Ott. A hybrid approach to atmospheric modeling that combines machine learning with a physics-based numerical model. *Journal of Advances in Modeling Earth Systems*, 14(3):e2021MS002712, 2022. doi:<https://doi.org/10.1029/2021MS002712>.
- Troy Arcomano, Istvan Szunyogh, Alexander Wikner, Brian R. Hunt, and Edward Ott. A hybrid atmospheric model incorporating machine learning can capture dynamical processes not captured by its physics-based component. *Geophysical Research Letters*, 50(8):e2022GL102649, 2023. doi:<https://doi.org/10.1029/2022GL102649>.
- Karumuri Ashok, Swadhin K. Behera, Suryachandra A. Rao, Hengyi Weng, and Toshio Yamagata. El niño modoki and its possible teleconnection. *Journal of Geophysical Research: Oceans*, 112(C11), 2007. doi:<https://doi.org/10.1029/2006JC003798>.
- Kaifeng Bi, Lingxi Xie, Hengheng Zhang, Xin Chen, Xiaotao Gu, and Qi Tian. Accurate medium-range global weather forecasting with 3d neural networks. *Nature*, 619(7970):533–538, 2023. doi:10.1038/s41586-023-06185-3.
- J. Bjerknes. Atmospheric teleconnections from the equatorial pacific. *Monthly Weather Review*, 97(3):163 – 172, 1969. doi:10.1175/1520-0493(1969)097<0163:ATFTEP>2.3.CO;2.
- G. B. Brassington, M. J. Martin, H. L. Tolman, S. Akella, M. Balmeseda, C. R. S. Chambers, E. Chassignet, J. A. Cummings, Y. Drillet, P. A. E. M. Jansen, P. Laloyaux, D. Lea, A. Mehra, I. Mirouze, H. Ritchie, G. Samson, P. A. Sandery, G. C. Smith, M. Suarez, and R. Todling. Progress and challenges in short- to medium-range coupled prediction. *Journal of Operational Oceanography*, 8(sup2):s239–s258, 2015. doi:10.1080/1755876X.2015.1049875.
- Ashesh Chattopadhyay and Pedram Hassanzadeh. Long-term instabilities of deep learning-based digital twins of the climate system: The cause and a solution, 2023.
- Kang Chen, Tao Han, Junchao Gong, Lei Bai, Fenghua Ling, Jing-Jia Luo, Xi Chen, Leiming Ma, Tianning Zhang, Rui Su, Yuanzheng Ci, Bin Li, Xiaokang Yang, and Wanli Ouyang. Fengwu: Pushing the skillful global medium-range weather forecast beyond 10 days lead, 2023a.
- Lei Chen, Xiaohui Zhong, Jie Wu, Deliang Chen, Shangping Xie, Qingchen Chao, Chensen Lin, Zixin Hu, Bo Lu, Hao Li, and Yuan Qi. Fuxi-s2s: An accurate machine learning model for global subseasonal forecasts, 2023b.
- Lei Chen, Xiaohui Zhong, Feng Zhang, Yuan Cheng, Yinghui Xu, Yuan Qi, and Hao Li. Fuxi: A cascade machine learning forecasting system for 15-day global weather forecast, 2023c.
- Allan J. Clarke and Stephen Van Gorder. Improving el niño prediction using a space-time integration of indo-pacific winds and equatorial pacific upper ocean heat content. *Geophysical Research Letters*, 30(7), 2003. doi:<https://doi.org/10.1029/2002GL016673>.
- Aiguo Dai and T. M. L. Wigley. Global patterns of enso-induced precipitation. *Geophysical Research Letters*, 27(9): 1283–1286, 2000. doi:<https://doi.org/10.1029/1999GL011140>.
- F.M. de Andrade, C.A.S. Coelho, and I.F.A. Cavalcanti. Global precipitation hindcast quality assessment of the subseasonal to seasonal (s2s) prediction project models. *Climate Dynamics*, 52:5451–5472, 2019. doi:<https://doi.org/10.1007/s00382-018-4457-z>.
- Daniela I. V. Domeisen, Christopher J. White, Hilla Afargan-Gerstman, Ángel G. Muñoz, Matthew A. Janiga, Frédéric Vitart, C. Ole Wulff, Salomé Antoine, Constantin Ardilouze, Lauriane Batté, Hannah C. Bloomfield, David J. Brayshaw, Suzana J. Camargo, Andrew Charlton-Pérez, Dan Collins, Tim Cowan, Maria del Mar Chaves, Laura

- Ferranti, Rosario Gómez, Paula L. M. González, Carmen González Romero, Johnna M. Infanti, Stelios Karozis, Hera Kim, Erik W. Kolstad, Emerson LaJoie, Llorenç Lledó, Linus Magnusson, Piero Malguzzi, Andrea Manrique-Suñén, Daniele Mastrangelo, Stefano Materia, Hanoi Medina, Lluís Palma, Luis E. Pineda, Athanasios Sfetsos, Seok-Woo Son, Albert Soret, Sarah Strazzo, and Di Tian. Advances in the subseasonal prediction of extreme events: Relevant case studies across the globe. *Bulletin of the American Meteorological Society*, 103(6):E1473 – E1501, 2022. doi:10.1175/BAMS-D-20-0221.1.
- E. S. Epstein. Stochastic dynamic prediction. *Tellus*, pages 739 – 759, 1969. doi:10.1111/j.2153-3490.1969.tb00483.x.
- Jean-Christophe Golaz, Luke P. Van Roekel, Xue Zheng, Andrew F. Roberts, Jonathan D. Wolfe, Wuyin Lin, Andrew M. Bradley, Qi Tang, Mathew E. Maltrud, Ryan M. Forsyth, Chengzhu Zhang, Tian Zhou, Kai Zhang, Charles S. Zender, Mingxuan Wu, Hailong Wang, Adrian K. Turner, Balwinder Singh, Jadwiga H. Richter, Yi Qin, Mark R. Petersen, Azamat Mametjanov, Po-Lun Ma, Vincent E. Larson, Jayesh Krishna, Noel D. Keen, Nicole Jeffery, Elizabeth C. Hunke, Walter M. Hannah, Oksana Guba, Brian M. Griffin, Yan Feng, Darren Engwirda, Alan V. Di Vittorio, Cheng Dang, LeAnn M. Conlon, Chih-Chieh-Jack Chen, Michael A. Brunke, Gautam Bisht, James J. Benedict, Xylar S. Asay-Davis, Yuying Zhang, Meng Zhang, Xubin Zeng, Shaocheng Xie, Phillip J. Wolfram, Tom Vo, Milena Veneziani, Teklu K. Tesfa, Sarat Sreepathi, Andrew G. Salinger, J. E. Jack Reeves Eyre, Michael J. Prather, Salil Mahajan, Qing Li, Philip W. Jones, Robert L. Jacob, Gunther W. Huebler, Xianglei Huang, Benjamin R. Hillman, Bryce E. Harrop, James G. Foucar, Yilin Fang, Darin S. Comeau, Peter M. Caldwell, Tony Bartoletti, Karthik Balaguru, Mark A. Taylor, Renata B. McCoy, L. Ruby Leung, and David C. Bader. The doe e3sm model version 2: Overview of the physical model and initial model evaluation. *Journal of Advances in Modeling Earth Systems*, 14(12):e2022MS003156, 2022. doi:https://doi.org/10.1029/2022MS003156.
- B. B. Goswami, B. Khouider, R. Phani, P. Mukhopadhyay, and A. J. Majda. Implementation and calibration of a stochastic multicloud convective parameterization in the ncep climate forecast system (cfsv2). *Journal of Advances in Modeling Earth Systems*, 9(3):1721–1739, 2017. doi:https://doi.org/10.1002/2017MS001014.
- YG. Ham, JH. Kim, and JJ. Luo. Deep learning for multi-year enso forecasts. *Nature*, 573:568–572, 2019. doi:10.1038/s41586-019-1559-7.
- Hans Hersbach, Bill Bell, Paul Berrisford, Shoji Hirahara, Andras Horanyi, Joaquín Muñoz Sabater, Julien Nicolas, Carole Peubey, Raluca Radu, Dinand Schepers, Adrian Simmons, Cornel Soci, Saleh Abdalla, Xavier Abellan, Gianpaolo Balsamo, Peter Bechtold, Gionata Biavati, Jean Bidlot, Massimo Bonavita, Giovanna De Chiara, Per Dahlgren, Dick Dee, Michail Diamantakis, Rossana Dragani, Johannes Flemming, Richard Forbes, Manuel Fuentes, Alan Geer, Leo Haimberger, Sean Healy, Robin J. Hogan, Elías Hólm, Marta Janisková, Sarah Keeley, Patrick Laloyaux, Philippe Lopez, Cristina Lupu, Gabor Radnoti, Patricia de Rosnay, Iryna Rozum, Freja Vamborg, Sebastien Villaume, and Jean-Noël Thépaut. The era5 global reanalysis. *Quarterly Journal of the Royal Meteorological Society*, 146(730):1999–2049, 2020. doi:https://doi.org/10.1002/qj.3803.
- H. Jaeger. The “echo state” approach to analysing and training recurrent neural networks. *GMD Report, German National Research Center for Information Technology*, 148, 2001.
- M. Ji and A. Leetmaa. Impact of data assimilation on ocean initialization and el niño prediction. *Monthly Weather Review*, 125(5):742–753, 1997. doi:https://doi.org/10.1175/1520-0493(1997)125<0742:IODAOO>2.0.CO;2.
- Dmitrii Kochkov, Janni Yuval, Ian Langmore, Peter Norgaard, Jamie Smith, Griffin Mooers, James Lottes, Stephan Rasp, Peter Düben, Milan Klöwer, Sam Hatfield, Peter Battaglia, Alvaro Sanchez-Gonzalez, Matthew Willson, Michael P. Brenner, and Stephan Hoyer. Neural general circulation models, 2023.
- F. Kucharski, F. Molteni, and A. Bracco. Decadal interactions between the western tropical pacific and the north atlantic oscillation. *Climate Dynamics*, 26:79–91, 2006. doi:https://doi.org/10.1007/s00382-005-0085-5.
- Anna Kwa, Spencer K. Clark, Brian Henn, Noah D. Brenowitz, Jeremy McGibbon, Oliver Watt-Meyer, W. Andre Perkins, Lucas Harris, and Christopher S. Bretherton. Machine-learned climate model corrections from a global storm-resolving model: Performance across the annual cycle. *Journal of Advances in Modeling Earth Systems*, 15(5):e2022MS003400, 2023. doi:https://doi.org/10.1029/2022MS003400.
- Andy Wang-Chun Lai, Michael Herzog, and Hans-F. Graf. Enso forecasts near the spring predictability barrier and possible reasons for the recently reduced predictability. *Journal of Climate*, 31(2):815 – 838, 2018. doi:10.1175/JCLI-D-17-0180.1.
- Remi Lam, Alvaro Sanchez-Gonzalez, Matthew Willson, Peter Wirnsberger, Meire Fortunato, Ferran Alet, Suman Ravuri, Timo Ewalds, Zach Eaton-Rosen, Weihua Hu, Alexander Merose, Stephan Hoyer, George Holland, Oriol Vinyals, Jacklynn Stott, Alexander Pritzel, Shakir Mohamed, and Peter Battaglia. Learning skillful medium-range global weather forecasting. *Science*, 382:1416–1421, 2023. doi:10.1126/science.adi2336.

- David A. Lavers, Adrian Simmons, Freja Vamborg, and Mark J. Rodwell. An evaluation of era5 precipitation for climate monitoring. *Quarterly Journal of the Royal Meteorological Society*, 148(748):3152–3165, 2022. doi:<https://doi.org/10.1002/qj.4351>.
- Sukyong Lee, Michelle L’Heureux, Andrew T. Wittenberg, Richard Seager, Paul A. O’Gorman, and Nathaniel C. Johnson. On the future zonal contrasts of equatorial pacific climate: Perspectives from observations, simulations, and theories. *npj Clim Atmos Sci*, 5(82), 2022. doi:10.1038/s41612-022-00301-2.
- C. E. Leith. Theoretical skill of monte carlo forecasts. *Monthly Weather Review*, 102(6):409 – 418, 1974. doi:10.1175/1520-0493(1974)102<0409:TSOMCF>2.0.CO;2.
- Shuhua Li and Andrew W. Robertson. Evaluation of submonthly precipitation forecast skill from global ensemble prediction systems. *Monthly Weather Review*, 143(7):2871 – 2889, 2015. doi:10.1175/MWR-D-14-00277.1.
- J. Lin and T. Qian. A new picture of the global impacts of el nino-southern. *Scientific Reports*, (9):17543, 2019. doi:10.1038/s41598-019-54090-5.
- Richard D. Lindzen. Planetary waves on beta-planes. *Monthly Weather Review*, 95(7):441 – 451, 1967. doi:10.1175/1520-0493(1967)095<0441:PWOBP>2.3.CO;2.
- Y. Liu, W. Cai, X. Lin, Z. Li, and Y. Zhang. Nonlinear el nino impacts on the global economy under climate change. *Nature Communications*, (14):5887, 2023. doi:10.1038/s41467-023-41551-9.
- T. Losada, B. Rodriguez-Fonseca, E. Mohino, J. Bader, S. Janicot, and C. R. Mechoso. Tropical sst and sahel rainfall: A non-stationary relationship. *Geophysical Research Letters*, 39(12), 2012. doi:<https://doi.org/10.1029/2012GL052423>.
- Mantas Lukoševičius. *A Practical Guide to Applying Echo State Networks*, pages 659–686. Springer Berlin Heidelberg, Berlin, Heidelberg, 2012. ISBN 978-3-642-35289-8. doi:10.1007/978-3-642-35289-8_36.
- Mantas Lukoševičius and Herbert Jaeger. Reservoir computing approaches to recurrent neural network training. *Computer Science Review*, 3(3):127–149, 2009. ISSN 1574-0137. doi:<https://doi.org/10.1016/j.cosrev.2009.03.005>.
- Simon J. Mason and Lisa Goddard. Probabilistic precipitation anomalies associated with en so. *Bulletin of the American Meteorological Society*, 82(4):619 – 638, 2001. doi:10.1175/1520-0477(2001)082<0619:PPAAWE>2.3.CO;2.
- Taroh Matsuno. Quasi-geostrophic motions in the equatorial area. *Journal of the Meteorological Society of Japan. Ser. II*, 44(1):25–43, 1966. doi:10.2151/jmsj1965.44.1_25.
- Michael J. McPhaden. Tropical pacific ocean heat content variations and enso persistence barriers. *Geophysical Research Letters*, 30(9), 2003. doi:<https://doi.org/10.1029/2003GL016872>.
- Michael J. McPhaden, Stephen E. Zebiak, and Michael H. Glantz. Enso as an integrating concept in earth science. *Science*, 314(5806):1740–1745, 2006. doi:10.1126/science.1132588.
- Andrea Molod, Eric Hackert, Yury Vikhliayev, Bin Zhao, Donifan Barahona, Guillaume Vernieres, Anna Borovikov, Robin M. Kovach, Jelena Marshak, Siegfried Schubert, Zhao Li, Young-Kwon Lim, Lauren C. Andrews, Richard Cullather, Randal Koster, Deepthi Achuthavarier, James Carton, Lawrence Coy, Julliana L. M. Friere, Karla M. Longo, Kazumi Nakada, and Steven Pawson. Geos-s2s version 2: The gmao high-resolution coupled model and assimilation system for seasonal prediction. *Journal of Geophysical Research: Atmospheres*, 125(5):e2019JD031767, 2020. doi:<https://doi.org/10.1029/2019JD031767>.
- F. Molteni. Atmospheric simulations using a gcm with simplified physical parametrizations. i: model climatology and variability in multi-decadal experiments. *Climate Dynamics*, 20:175–191, 2003. doi:<https://doi.org/10.1007/s00382-002-0268-2>.
- S. Monhart, C. Spirig, J. Bhend, K. Bogner, C. Schär, and M. A. Liniger. Skill of subseasonal forecasts in europe: Effect of bias correction and downscaling using surface observations. *Journal of Geophysical Research: Atmospheres*, 123(15):7999–8016, 2018. doi:<https://doi.org/10.1029/2017JD027923>.
- S. Mouatadid, P. Orenstein, G. Flaspohler, J. Cohen, M. Oprescu, E. Fraenkel, and L. Mackey. Adaptive bias correction for improved subseasonal forecasting. *Nature Communications*, 14:3482, 2023. doi:<https://doi.org/10.1038/s41467-023-38874-y>.
- National Academies of Sciences and Engineering and Medicine. *Next Generation Earth System Prediction: Strategies for Subseasonal to Seasonal Forecasts*. The National Academies Press, Washington, DC, 2016. ISBN 978-0-309-38880-1. doi:10.17226/21873.
- Tung Nguyen, Rohan Shah, Hritik Bansal, Troy Arcomano, Sandeep Madireddy, Romit Maulik, Veerabhadra Kotamarthi, Ian Foster, and Aditya Grover. Scaling transformer neural networks for skillful and reliable medium-range weather forecasting, 2023.
- R G Owens and T D Hewson. Ecmwf forecast user guide. reading: Ecmwf., 2018.

- Dhruvit Patel and Edward Ott. Using machine learning to anticipate tipping points and extrapolate to post-tipping dynamics of non-stationary dynamical systems. *Chaos: An Interdisciplinary Journal of Nonlinear Science*, 33(2): 023143, 02 2023. ISSN 1054-1500. doi:10.1063/5.0131787.
- J. Pathak, S. Subramanian, P. Harrington, S. Raja, A. Chattopadhyay, M. Mardani, T. Kurth, D. Hall, Z. Li, K. Aziz-zadenesheli, P. Hassanzadeh, K. Kashinath, and A. Anandkumar. Fourcastnet: A global data-driven high-resolution weather model using adaptive fourier neural operators. *arXiv*, 2022. doi:https://doi.org/10.48550/arXiv.2202.11214.
- Jaideep Pathak, Brian Hunt, Michelle Girvan, Zhixin Lu, and Edward Ott. Model-free prediction of large spatiotemporally chaotic systems from data: A reservoir computing approach. *Phys. Rev. Lett.*, 120:024102, Jan 2018a. doi:10.1103/PhysRevLett.120.024102.
- Jaideep Pathak, Alexander Wikner, Rebeckah Fussell, Sarthak Chandra, Brian R. Hunt, Michelle Girvan, and Edward Ott. Hybrid forecasting of chaotic processes: Using machine learning in conjunction with a knowledge-based model. *Chaos: An Interdisciplinary Journal of Nonlinear Science*, 28(4):041101, 2018b. ISSN 1054-1500. doi:10.1063/1.5028373.
- Stephan Rasp, Michael S. Pritchard, and Pierre Gentine. Deep learning to represent subgrid processes in climate models. *Proceedings of the National Academy of Sciences*, 115(39):9684–9689, 2018. doi:10.1073/pnas.1810286115.
- C. F. Ropelewski and M. S. Halpert. Global and regional scale precipitation patterns associated with the el niño/southern oscillation. *Monthly Weather Review*, 115(8):1606 – 1626, 1987. doi:10.1175/1520-0493(1987)115<1606:GARSPP>2.0.CO;2.
- I. Roy, A.S. Gagnon, and D. Siingh. Evaluating enso teleconnections using observations and cmip5 models. *Theoretical and Applied Climatology*, 136:1085–1098, 2019. doi:https://doi.org/10.1007/s00704-018-2536-z.
- Suranjana Saha, Shrinivas Moorthi, Xingren Wu, Jiande Wang, Sudhir Nadiga, Patrick Tripp, David Behringer, Yu-Tai Hou, Hui-ya Chuang, Mark Iredell, Michael Ek, Jesse Meng, Rongqian Yang, Malaquías Peña Mendez, Huug van den Dool, Qin Zhang, Wanqiu Wang, Mingyue Chen, and Emily Becker. The ncep climate forecast system version 2. *Journal of Climate*, 27(6):2185–2208, 2014. doi:https://doi.org/10.1175/JCLI-D-12-00823.1.
- Adam H. Sobel, Chia-Ying Lee, Steven G. Bowen, Suzana J. Camargo, Mark A. Cane, Amy Clement, Boniface Fosu, Megan Hart, Kevin A. Reed, Richard Seager, and Michael K. Tippett. Near-term tropical cyclone risk and coupled earth system model biases. *Proceedings of the National Academy of Sciences*, 120(33):e2209631120, 2023. doi:10.1073/pnas.2209631120.
- Istvan Szunyogh. *Applicable Atmospheric Dynamics*. WORLD SCIENTIFIC, 2014. doi:10.1142/8047.
- Gouhei Tanaka, Tadayoshi Matsumori, Hiroaki Yoshida, and Kazuyuki Aihara. Reservoir computing with diverse timescales for prediction of multiscale dynamics. *Phys. Rev. Res.*, 4:L032014, 2022. doi:10.1103/PhysRevResearch.4.L032014.
- A. N. Tikhonov and V. Y. Arsenin. Solutions of ill-posed problems. *Winston, Halsted Press*, 1977.
- A. Timmermann, SI. An, and JS. et al. Kug. El nino-southern oscillation complexity. *Nature*, (559):535–545, 2018. doi:10.1038/s41586-018-0252-6.
- Frédéric Vitart. Evolution of ecmwf sub-seasonal forecast skill scores. *Quarterly Journal of the Royal Meteorological Society*, 140(683):1889–1899, 2014. doi:https://doi.org/10.1002/qj.2256. URL https://doi.org/10.1002/qj.2256.
- Bin Wang, Jian Liu, Hyung-Jin Kim, Peter J. Webster, So-Young Yim, and Baoqiang Xiang. Northern hemisphere summer monsoon intensified by mega-el niño/southern oscillation and atlantic multidecadal oscillation. *Proceedings of the National Academy of Sciences*, 110(14):5347–5352, 2013. doi:10.1073/pnas.1219405110.
- Oliver Watt-Meyer, Noah D. Brenowitz, Spencer K. Clark, Brian Henn, Anna Kwa, Jeremy McGibbon, W. Andre Perkins, and Christopher S. Bretherton. Correcting weather and climate models by machine learning nudged historical simulations. *Geophysical Research Letters*, 48(15):e2021GL092555, 2021. ISSN 0094-8276. doi:https://doi.org/10.1029/2021GL092555.
- Jonathan A. Weyn, Dale R. Durran, Rich Caruana, and Nathaniel Cresswell-Clay. Sub-seasonal forecasting with a large ensemble of deep-learning weather prediction models. *Journal of Advances in Modeling Earth Systems*, 13(7): e2021MS002502, 2021. doi:https://doi.org/10.1029/2021MS002502.
- Matthew Wheeler and George N. Kiladis. Convectively coupled equatorial waves: Analysis of clouds and temperature in the wavenumber–frequency domain. *Journal of the Atmospheric Sciences*, 56(3):374 – 399, 1999. doi:10.1175/1520-0469(1999)056<0374:CCEWAO>2.0.CO;2.

- Christopher J. White, Henrik Carlsen, Andrew W. Robertson, Richard J. T. Klein, Jeffrey K. Lazo, Arun Kumar, Frederic Vitart, Erin Coughlan de Perez, Andrea J. Ray, Virginia Murray, Sukaina Bharwani, Dave MacLeod, Rachel James, Lora Fleming, Andrew P. Morse, Bernd Eggen, Richard Graham, Erik Kjellström, Emily Becker, Kathleen V. Pegion, Neil J. Holbrook, Darryn McEvoy, Michael Depledge, Sarah Perkins-Kirkpatrick, Timothy J. Brown, Roger Street, Lindsey Jones, Tomas A. Remenyi, Indi Hodgson-Johnston, Carlo Buontempo, Rob Lamb, Holger Meinke, Berit Arheimer, and Stephen E. Zebiak. Potential applications of subseasonal-to-seasonal (s2s) predictions. *Meteorological Applications*, 24(3):315–325, 2017. doi:10.1002/met.1654.
- Christopher J. White, Daniela I. V. Domeisen, Nachiketa Acharya, Elijah A. Adefisan, Michael L. Anderson, Stella Aura, Ahmed A. Balogun, Douglas Bertram, Sonia Bluhm, David J. Brayshaw, Jethro Browell, Dominik Büeler, Andrew Charlton-Perez, Xandre Chourio, Isadora Christel, Caio A. S. Coelho, Michael J. DeFlorio, Luca Delle Monache, Francesca Di Giuseppe, Ana María García-Solórzano, Peter B. Gibson, Lisa Goddard, Carmen González Romero, Richard J. Graham, Robert M. Graham, Christian M. Grams, Alan Halford, W. T. Katty Huang, Kjeld Jensen, Mary Kilavi, Kamoru A. Lawal, Robert W. Lee, David MacLeod, Andrea Manrique-Suñén, Eduardo S. P. R. Martins, Carolyn J. Maxwell, William J. Merryfield, Ángel G. Muñoz, Eniola Olaniyan, George Otieno, John A. Oyedepo, Lluís Palma, Ilias G. Pechlivanidis, Diego Pons, F. Martin Ralph, Dirceu S. Reis, Tomas A. Remenyi, James S. Risbey, Donald J. C. Robertson, Andrew W. Robertson, Stefan Smith, Albert Soret, Ting Sun, Martin C. Todd, Carly R. Tozer, Francisco C. Vasconcelos, Ilaria Vigo, Duane E. Waliser, Fredrik Wetterhall, and Robert G. Wilson. Advances in the application and utility of subseasonal-to-seasonal predictions. *Bulletin of the American Meteorological Society*, 103(6):E1448–E1472, 2022. doi:https://doi.org/10.1175/BAMS-D-20-0224.1.
- Alexander Wikner, Jaideep Pathak, Brian Hunt, Michelle Girvan, Troy Arcomano, Istvan Szunyogh, Andrew Pomerance, and Edward Ott. Combining machine learning with knowledge-based modeling for scalable forecasting and subgrid-scale closure of large, complex, spatiotemporal systems. *Chaos: An Interdisciplinary Journal of Nonlinear Science*, 30(5):053111, 2020. ISSN 1054-1500. doi:10.1063/5.0005541.
- Hojun You, Jiayi Wang, Raymond K. W. Wong, Courtney Schumacher, R. Saravanan, and Mikyoung Jun. Prediction of tropical pacific rain rates with over-parameterized neural networks, 2024.
- Chidong Zhang. Madden–julian oscillation: Bridging weather and climate. *Bulletin of the American Meteorological Society*, 94(12):1849–1870, 2013. doi:https://doi.org/10.1175/BAMS-D-12-00026.1.
- Lujun Zhang, Taareem Kim, Tiantian Yang, Yang Hong, and Qian Zhu. Evaluation of subseasonal-to-seasonal (s2s) precipitation forecast from the north american multi-model ensemble phase ii (nmme-2) over the contiguous u.s. *Journal of Hydrology*, 603:127058, 2021. ISSN 0022-1694. doi:https://doi.org/10.1016/j.jhydrol.2021.127058.
- Tongtiegang Zhao, Yongyong Zhang, and Xiaohong Chen. Predictive performance of nmme seasonal forecasts of global precipitation: A spatial-temporal perspective. *Journal of Hydrology*, 570:17–25, 2019. ISSN 0022-1694. doi:https://doi.org/10.1016/j.jhydrol.2018.12.036.
- Fei Zheng and Jiang Zhu. Spring predictability barrier of enso events from the perspective of an ensemble prediction system. *Global and Planetary Change*, 72(3):108–117, 2010. ISSN 0921-8181. doi:https://doi.org/10.1016/j.gloplacha.2010.01.021.
- Lu Zhou and Rong-Hua Zhang. A self-attention-based neural network for three-dimensional multivariate modeling and its skillful enso predictions. *Science Advances*, 9(10):eadf2827, 2023. doi:10.1126/sciadv.adf2827.
- H. Zuo, M. A. Balmaseda, S. Tietsche, K. Mogensen, and M. Mayer. The ecmwf operational ensemble reanalysis–analysis system for ocean and sea ice: a description of the system and assessment. *Ocean Science*, 15(3):779–808, 2019. doi:10.5194/os-15-779-2019.